Workshop of

CODE_BRIGHT USERS

22 September 2021
Barcelona, Spain

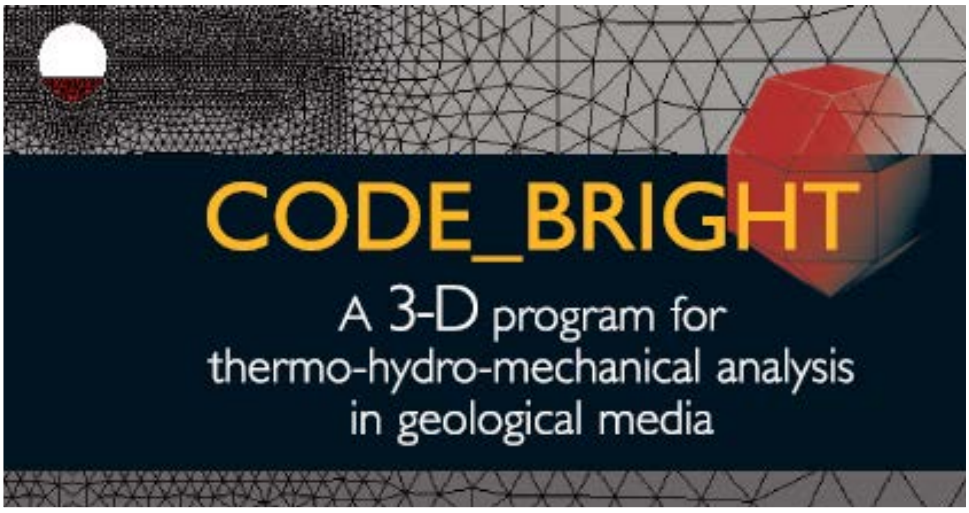

Department of Civil and Environmental Engineering
UPC-BarcelonaTech
Barcelona, Spain

CIMNE
International Center for Numerical Methods in Engineering
Barcelona, Spain

CODE_BRIGHT

A 3-D program for thermo-hydro-mechanical analysis in geological media

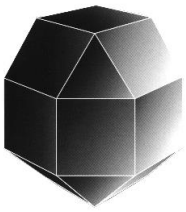

WORKSHOP OF CODE_BRIGHT USERS

Barcelona, 22 September 2021

Department of Civil and Environmental Engineering

(UPC-BarcelonaTech, Barcelona, Spain)

CIMNE

(International Center for Numerical Methods in Engineering, Barcelona, Spain)

CONTENTS

Challenges in 3D - THM Modelling of Final Disposal Repository For Nuclear Spent Fuel

Erdem Toprak[1], Sebastia Olivella[2] and Xavier Pintado[3]

[1] International Center for Numerical Methods in Engineering (CIMNE), Universitat Politècnica de Catalunya (UPC) Campus Nord, 08034 Barcelona, Spain
E-mail: erdem.toprak@upc.edu

[2] Department of Civil and Environmental Engineering (DECA), Universitat Politècnica de Catalunya (UPC) Campus Nord, 08034 Barcelona, Spain
E-mail: sebastia.olivella@upc.edu, E-mail: jordi.alcoverro@upc.edu

[3] Ains Group, Bertel Jungin aukio 9, 02600 Espoo, Finland
E-mail: xavier.pintado@ains.fi

Key words: 3D - THM calculations, BBM – linear approach, 3D – TH boundary conditions, 3D THM modelling of FISST, 3D HM modelling of PGZ Test, challenges in 3D calculations.

Abstract: *Disposal of spent fuel in an underground repository should be studied to understand processes taking place for long-term conditions. The thermo-hydro-mechanical modelling is intended to give an answer about temperatures achieved, saturation times and pore pressure developments, and displacements and stresses caused by swelling of barrier components. This paper describes challenges for 3D - THM modelling of Engineered Barrier Systems (EBS) in disposal schemes, 3D THM modelling of FISST and 3D HM modelling of a big scale gas injection test (PGZ). Difficulties encountered are, among other aspects, related to mechanical constitutive modelling, boundary condition application, geometry preparation and meshing.*

1 INTRODUCTION

There are three modelling work has been discussed in this paper:

- 3D THM Simulations for Predicting Evolution of Underground Radioactive Waste Disposal (Toprak et al., 2020) : The simulations presented in this study are used to check performance of the bentonite barriers in final disposal facility in base case and in mentioned sensitivity analyses. Performance targets related to swelling pressure limits, buffer upheave, hydraulic conductivity and temperature are checked. Moreover, saturation times and time until bentonite achieves its performance are obtained in different background conditions.
- THM Calculations for FISST (Toprak et al., 2019): Posiva is planning a number of demonstration tests in ONKALO. The Full-scale In Situ System Test (FISST) is an ongoing project. The FISST is instrumented in order to measure the evolution of the temperature, hydration and the development of mechanical response; for example: swelling pressure. In this study, results of THM calculations for a complete drift with two deposition holes are presented.
- 3D HM Modelling of Big Scale PGZ Test : In order to understand gas migration from engineered barrier system to host rock (gas migration mechanism into COx) and gas pathway development along the host rock; PGZ experiments (De La Vaissière, 2010) have been selected as reference experiments. In this document (Toprak et al., 2021), prelaminar modelling of PGZ1 experiment has been discussed.

2 CHALLENGES and SIMPLIFICATIONS IN 3D THM MODELLING

Barcelona Basic Model (BBM) is widely used to simulate the HM behavior of unsaturated soils. An extension for temperature effects and materials undergoing significant expansion is also available. However, this type of models are highly nonlinear by definition. Figure 1-A displays the net stress - suction path during hydration at constant volume. While the original model (BBM) concentrates swelling close to full saturation, the model extension for expansive material (BBM-Ex) can produce other type of response depending on the parameters calibrated. The complexity of the nonlinear functions used in BBM and BBMEx might imply a computational cost dramatically high for a model representing a repository in 3D. In other words, it may require too small time steps. The size of the time step is controlled by, thermal flow, hydration and expansion which change in space and time.

Linearization of mechanical model permits to reduce the computational cost in the numerical calculation. The linearization approach maintains the same deformational processes, i.e. deformations are due to stress, suction and temperature; and it is advantageous to carry out complex geometrical 3D calculations. Figure 1-A shows that in linear model, it is possible to obtain a response with the same swelling pressure as obtained with BBM (Original or Expansive).

The THM processes involved in a repository have different characteristic lengths. For thermal and hydraulic problems, it is necessary to involve a large volume or rock. Heat and water flow propagate to large distances. In contrast, the mechanical part is more local. This implies that TH modelling can be done in a large domain previously to the THM calculation. This may permit to set TH conditions for upper, lower and lateral boundaries in a reduced 3D geometry (Figure 1-B and Figure 2-B). Variable temperature and liquid pressure determined from the TH large domain model calculations can be imposed on boundaries of a reasonably reduced 3D geometry (Figure 1-B and Figure 2-B).

Generation of geometry and meshing is also an important issue in 3D - THM calculations. It must be noted that linear tetrahedra are not the best option in some materials. There are several reasons, one is incompressibility and another is the inability to reproduce gradients correctly in case of relatively coarse meshes. To deal with this issue, a detailed geometry must be created so hexahedra can be used in the mesh. A proper generated geometry with structured mesh (Figure 1-B and Figure 2-B) permits hexahedra elements and has a positive effect on gradients and deformations for 3D – THM calculations.

Figure 3 shows layout of the experiment (A) and the model (B). There are three drifts considered in the model geometry: GMR, GED and GED. The test consists of an injection borehole (PGZ1201), a borehole for monitoring interstitial pressures (PGZ1202), and a borehole for monitoring rock deformation (PGZ1031). The injection borehole (PGZ1201) has been incorporated to the geometry as a separate material instead of boundary condition. In the model, the boreholes have been represented as line elements. Only, interval 2 (where the gas injection takes place) of injection borehole (PGZ1201) has been meshed. As the boreholes are inclined, structured mesh is not possible in this model. Semi-structured mesh has been assigned to whole geometry.

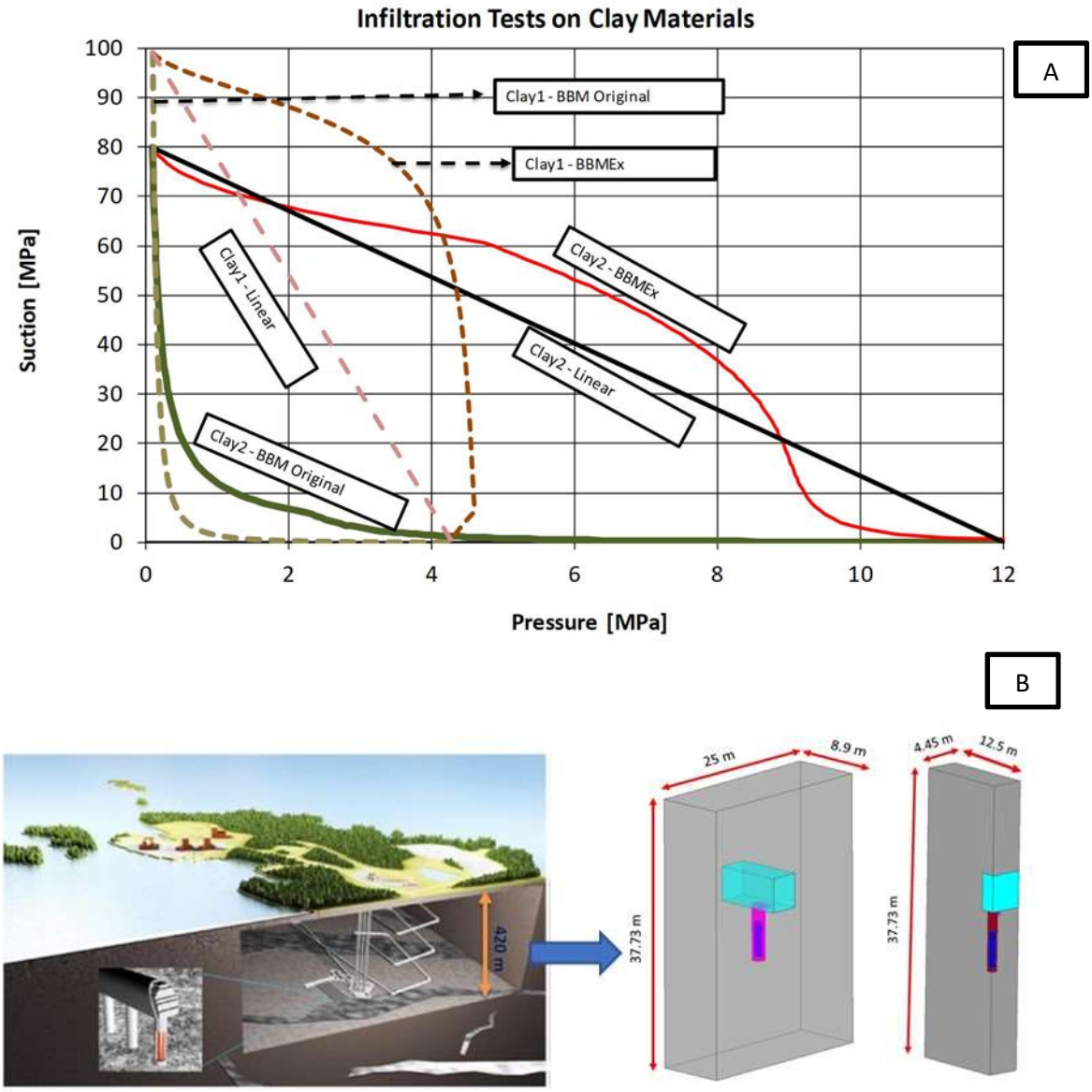

Figure 1. Linear approach to represent expansive materials (A), an example of continuous geometry for 3D THM calculations (B) (Toprak et al., 2020)

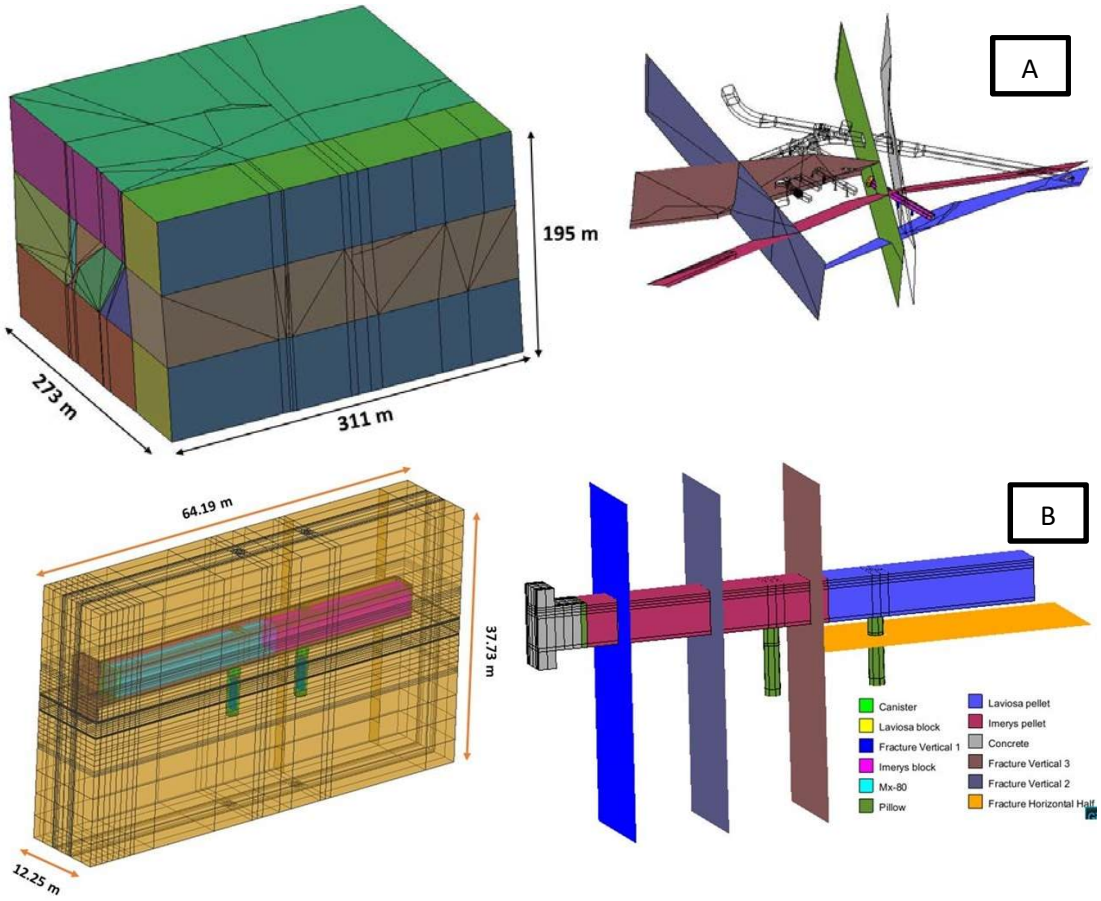

Figure 2. Fractures and location of test (A, figure from Posiva) and simplification of FISST geometry for THM calculations (Toprak et al., 2019)

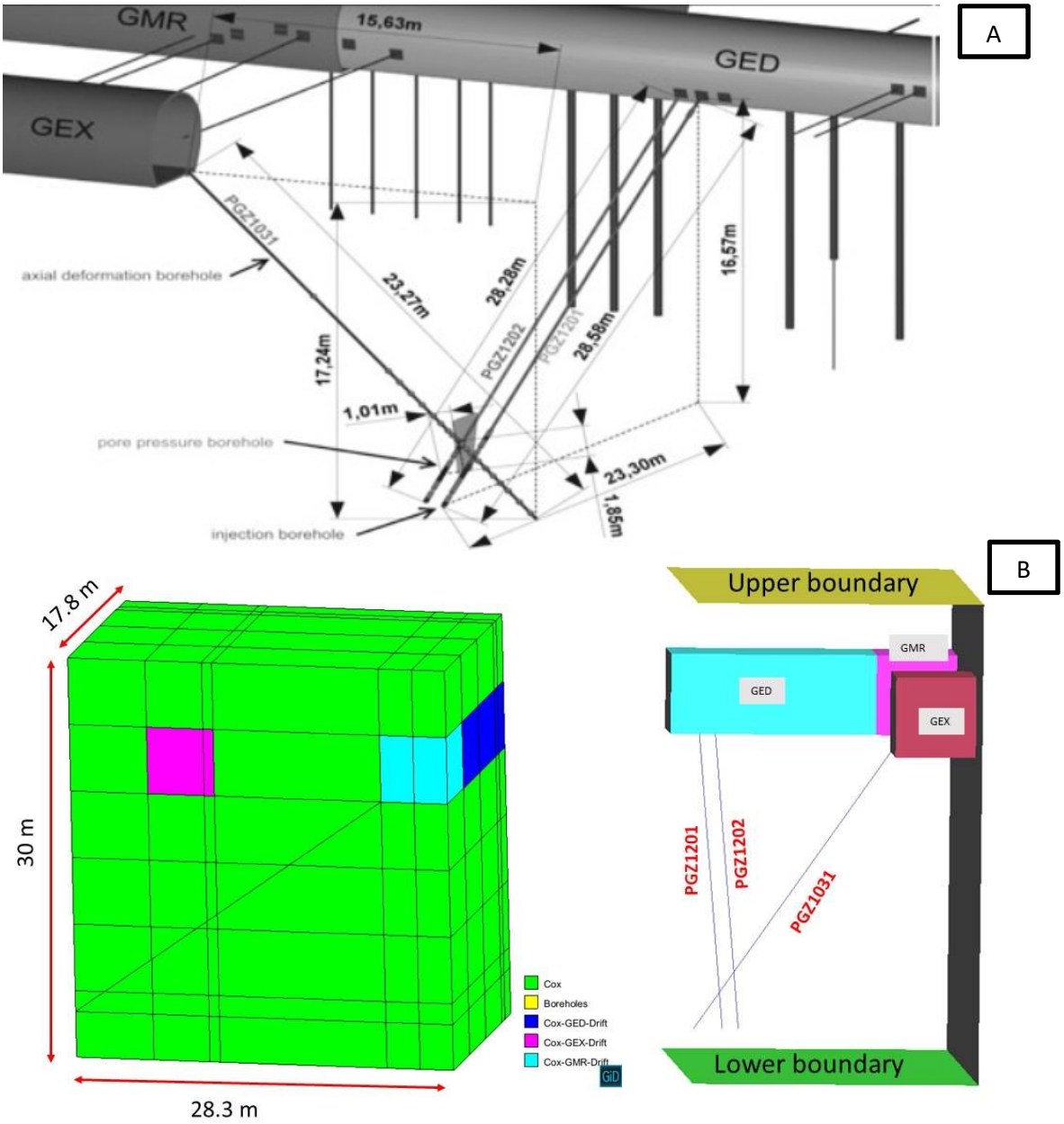

Figure 3. PGZ test geometry (A, figure from Andra) and simplified 3D geometry for HM calculations (Toprak et al., 2021).

3 CONCLUSIONS

In this paper, challenges in 3D THM modelling, in the context of nuclear waste repository, has been discussed. In big geometries (for example FISST geometry), instead of complex mechanical model, linear approach has been used to simulate mechanical behavior of materials (Toprak et al., 2019).

For 3D sensitivity analyses (Toprak et al.,2020); a continuous geometry (quarter) with a structured mesh has been used. As the geometry has been significantly reduced, BBM could have been used as mechanical model for bentonite. Hydraulic calculations for canister were not coupled.

In order to simulate PGZ test (De La Vaissière, 2010), inclined boreholes have been incorporated to geometry as line elements instead of small volumes. Only the gas injection location has been meshed in the gas injection borehole. The geometry has been prepared as continuous as possible. Semi-structured mesh has been used. HM modelling of PGZ test is an ongoing study.

ACKNOWLEDGEMENTS

This work was supported by Posiva Oy, AINS Group and EURAD.

REFERENCES

i. De La Vaissière, R., (2010) Design and Installation of the PGZ1 Experiment at Bure. FORGE Report D5.4 – VER.0

ii. Toprak, E., Olivella, S., Alcoverro, J., Pintado, X. (2019). THM calculations for FISST. Eurajoki, Finland: Posiva Oy. Technical Memorandum, kronodoc. POS-031471.

iii. Toprak, E., Olivella, S. Pintado, X. (2020) 3D THM Simulations For Predicting Evolution Of Underground Radioactive Waste Disposal. *Under preparation.*

iv. Toprak, E., Olivella, S. (2021) Preliminary HM Modelling of PGZ Test. EURAD Milestone 124 and 125: Experimental progress report of task 3.1 / 3.2 and on modelling progress (task 3.3).

3D GAS INJECTION SIMULATIONS ON CALLOVO OXFORDIAN CLAYSTONE USING A SPATIALLY CORRELATED HETEROGENEOUS MODEL

Yunfeng Zhou*, Alfonso Rodriguez-Dono* and Sebastia Olivella*

* Department of Civil and Environmental Engineering
Universitat Politècnica de Catalunya (UPC)
Campus Nord UPC, 08034 Barcelona, Spain

Key words: Gas migration, Callovo Oxfordian (COx) claystone, heterogeneous model, embedded fracture model, preferential pathways, CODE_BRIGHT.

Abstract. *Gas injection simulations are performed using a spatially correlated heterogeneous model. A matrix decomposition technique is adopted to generate a structured and random field of porosity. An exponential law combined with a cubic law is incorporated in the heterogeneous model. Both models have been implemented in the Finite Element Method software CODE_BRIGHT. Tentative three-dimensional gas migration simulations considering the influence of range, mesh and seed are conducted on Callovo-Oxfordian (COx) claystone. Preliminary results are compared with the laboratory results.*

1 INTRODUCTION

Callovo-Oxfordian (COx) claystone has been selected as a possible host rock by the French agency for the management of radioactive waste (Andra) [1]. One significant issue is to understand the mechanisms of gas transport through the host rock. Gas flow experiments have been conducted on COx by the British Geological Survey [2]. A 3D hydro-gas-mechanical model is introduced to simulate the experiment. A spatially connected heterogeneous sample is generated through the LU decomposition approach [3].

2 EXPERIMENT DESCRIPTION

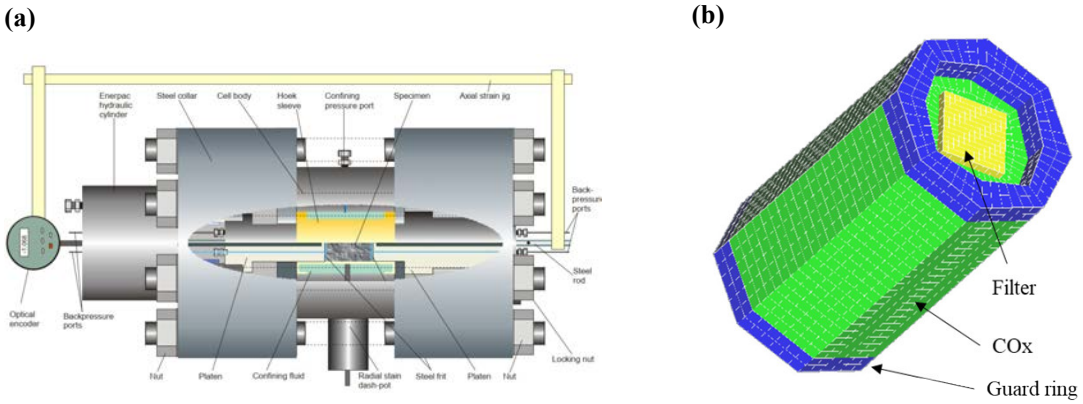

Figure 1 (a) Schematic of gas flow experiment apparatus and (b) model geometry [2].

Figure 1 presents the experimental set-up for gas flow on COx. A constant radial stress of 12.5 MPa (13 MPa in the axial direction) is imposed to the COx sample through the surrounding fluid media, and the initial pore pressure was 4.5 MPa. The injection location is

axially centred through a filter. Gas pressure is imposed at the injection boundary and gas flow rates are measured. There is also no restriction on the development of volumetric strains.

Details about experiment data and boundary conditions can be referred to [2, 4].

3 MODEL DESCRIPTION

3.1 Heterogeneous model [3]

If C is the covariance matrix of $N1$ grid points to simulate. It is positive-definite and can be decomposed into upper and lower triangular matrices (Cholesky algorithm).

$$C = L \cdot U \; with \; L = U^T \tag{1}$$

ω is a vector of $N1$ independent normally distributed random numbers. The vector y can be defined as:

$$y = L \cdot \omega \tag{2}$$

The mean and covariance of the random variable Y corresponding to y are obtained:

$$E(Y) = 0 \tag{3}$$

$$Cov(Y) = E(L\omega(L\omega)^T) = L \cdot E(\omega\omega^T) \cdot U = C \tag{4}$$

If the spherical covariance model is adopted below:

$$\begin{aligned} C(0) &= C_0 + C_1, \; h = 0 \\ C(h) &= C_1[1 - 1.5(h/a) + 0.5(h/a)^3], \; 0 < h \leq a \\ C(h) &= 0, \; h > a \end{aligned} \tag{5}$$

Where C_0 is the nugget, which is due both to measurement errors and to micro-variabilities of the mineralization; a denotes the range, which means that any data value will be correlated with any other value falling within a radius a (as shown in Figure 2); h is the distance between two elements.

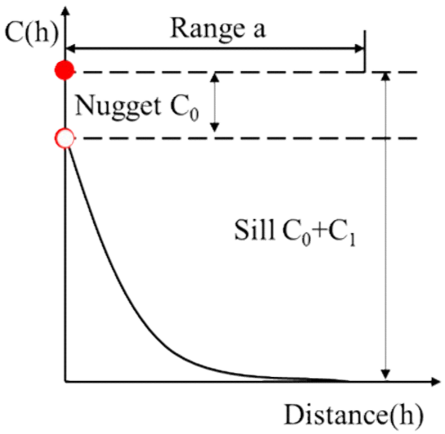

Figure 2 Schematic of the covariance model.

Then, vector y is therefore the autocorrelated simulation with the covariance model C.

If we generate a random field for porosity (ϕ) with the mean m and covariance C, and the range is a, it can be derived by:

$$\phi = y + m \tag{6}$$

The mean and covariance are given by:

$$E(\phi) = m,\ Cov(\phi) = C \tag{7}$$

The heterogeneous model is porosity-based, and the porosity obeys the gaussian random distribution.

3.2 Mechanical and hydraulic constitutive models

The mechanical model is based on linear elasticity. The global intrinsic permeability is defined as a function of material matrix and internal fracture permeabilities. The matrix permeability component is defined by (8).The constitutive equations of the embedded fracture model assumed can be referred to [5]. Parts of model properties are specified in Table 1. More details can be found in [4].

$$\boldsymbol{k} = \boldsymbol{k}_0 \exp\left(b(\phi - \phi_0)\right) \tag{8}$$

Where $\boldsymbol{k}_0$ is the initial permeability; b denotes a parameter to calibrate with the experiment data; ϕ and ϕ_0 are porosity for each element and reference porosity, respectively.

Parameters		Units	Values
Initial porosity	Average	—	0.15
	Variance	—	1×10^{-4}
Matrix Permeability, parallel	$k_{11}=k_{22}$	m^2	3.2×10^{-20}
Matrix Permeability, perpendicular	k_{33}	m^2	4.0×10^{-21}
Reference porosity	ϕ_0	—	0.15
Initial aperture	b_0	m	1.5×10^{-9}
Spacing	a	m	5.0×10^{-6}
Threshold strain	ε_0	—	5×10^{-4}
Maximum aperture	$b_{\max}$	m	1.5×10^{-7}
Tortuosity parameter	τ	—	0.05

Table 1 Model properties for COx.

3.3 Simulation schemes

#	Range	mesh	seed
Case 1a	0.0294	7392	0
Case 1b	1×10^{-20}		
Case 1c	0.0507		
Case 2a		14496	
Case 2b		21600	
Case 3a			100
Case 3b			1000

Table 2 List of cases to analyse the effect of material heterogeneity.

Three factors (Range, mesh and seed) are considered to generate different pore structures. The simulation schemes are listed in Table 2. Range represents the spatially correlated length of the heterogeneous field. It is worth noting that if the range is smaller than the smallest mesh size (Case 1b), a field is obtained without correlation. The heterogeneous field structure changes with different meshes and seeds. Examples for heterogeneous fields are displayed in Figure 3.

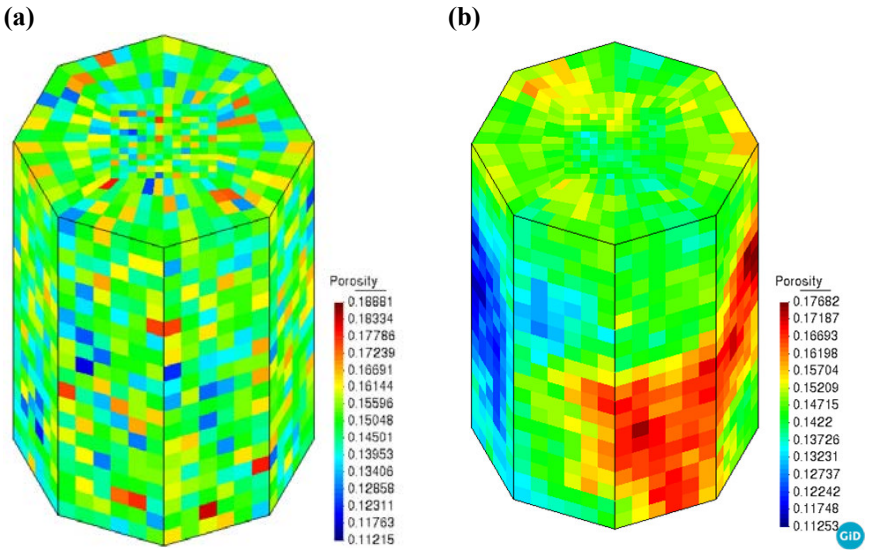

Case 1b Case 1c

Figure 3 Heterogeneous model for Case 1b and Case 1c.

4 RESULTS

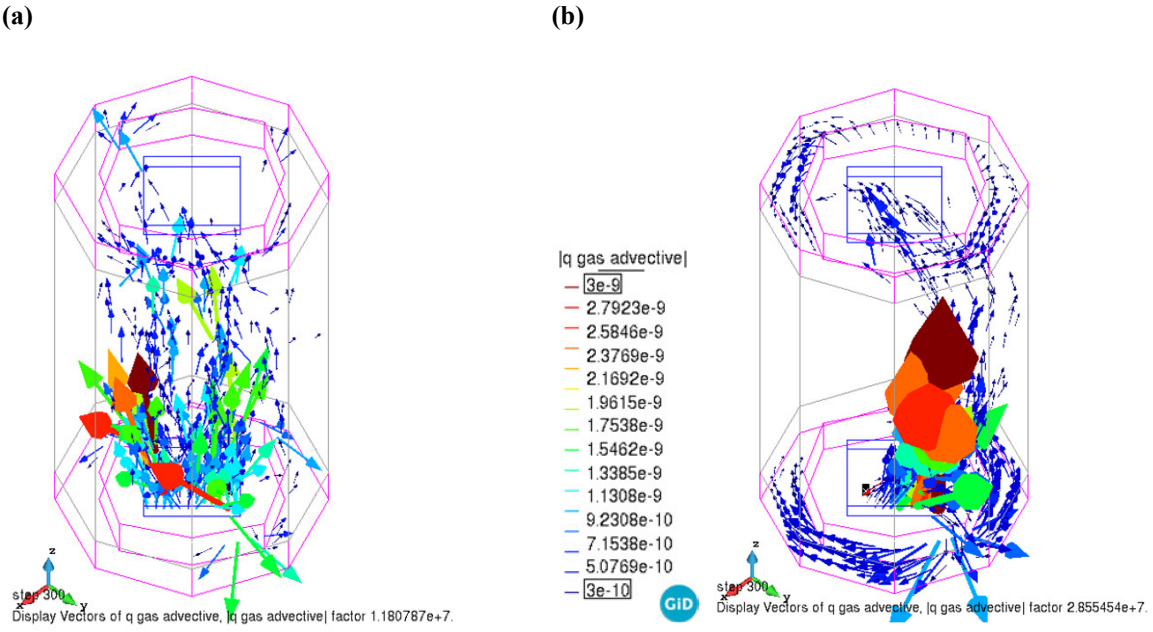

Case 1b Case 1c

Figure 4 Comparison between gas advective vectors at 300 days.

Figure 4 shows gas advective vectors for Case 1b and Case 1c. Preferential pathways can be observed. Flux vectors are more discrete in Case 1b while are oriented in the axial direction. Figure 5 shows gas pressure at filter and guard ring. Results for Case 1c show a reasonable agreement with measurements. Figure 6 presents gas inflow and outflow rate during gas injection. All the simulation results are lower than experiment data, and similar results are shown in Figure 7. The maximum volumetric strain in each case is almost half of the experiment data, but there is no decrease in volume.

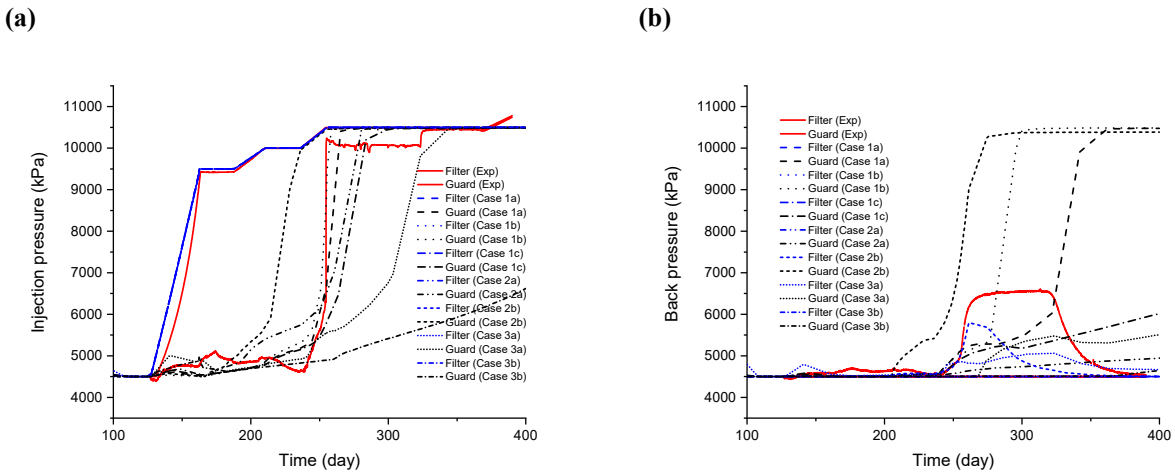

Figure 5 Comparison of injection pressure (a) and back pressure (b) at filter and guard ring with experiment data.

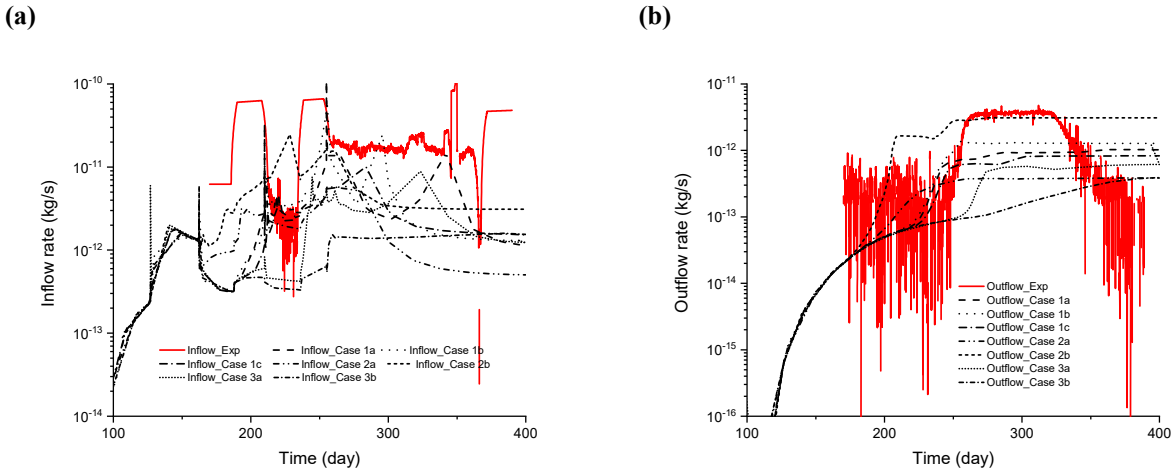

Figure 6 Comparison of gas flow rate with experiment data.

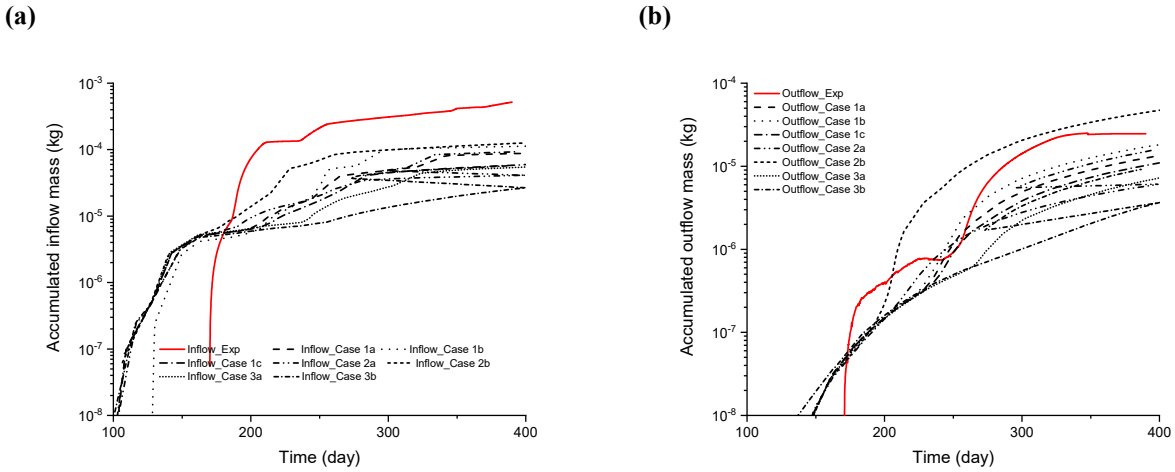

Figure 7 Comparison of accumulated gas flow into (a) and out (b) the COx specimen with experiment data.

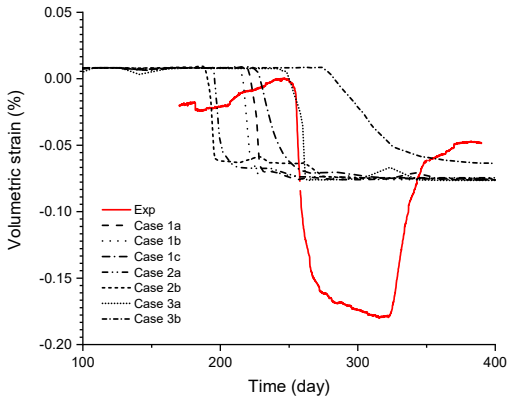

Figure 8 Comparison of volumetric strain with measurements.

4 CONCLUSIONS

- A preliminary study of gas migration in COx has been performed.
- A spatially heterogeneous filed can be generated automatically in CODE_BRIGHT, which provides a possible tool to study issues with heterogeneity.
- The effect of range, mesh and seed has been studied.
- Preferential paths can be observed by the proposed model. More sensitivity analysis will be conducted to explore the possibility of gas migration on COx.

REFERENCES

1. Menaceur, H., et al., *The thermo-mechanical behaviour of the Callovo-Oxfordian claystone.* International Journal of Rock Mechanics and Mining Sciences, 2015. **78**: p. 290-303.
2. Cuss, R. and J. Harrington, *Update on dilatancy associated with onset of gas flow in callovo-oxfordian claystone. Progress report on test SPP_COx-2.* 2011.
3. Davis, M.W., *Production of conditional simulations via the LU triangular decomposition of the covariance matrix.* Mathematical geology, 1987. **19**(2): p. 91-98.
4. Damians, I.P. and S. Olivella, *Decovalex-2019 (Task A Final Report-Annex A)*. 2020, Lawrence Berkeley National Lab.(LBNL), Berkeley, CA (United States).
5. Arnedo, D., et al., *Gas injection tests on sand/bentonite mixtures in the laboratory. Experimental results and numerical modelling.* Physics and Chemistry of the Earth, Parts A/B/C, 2008. **33**: p. S237-S247.

A BURGERS-VISCOPLASTIC STRAIN-SOFTENING CONSTITUTIVE MODEL FOR ROCKS

Fei Song[*], Alfonso Rodriguez-Dono[*†] and Sebastia Olivella[*]

[*] Department of Civil and Environmental Engineering
Technical University of Catalonia (UPC)
Campus Nord UPC, 08034 Barcelona, Spain

[†] Institute of Environmental Assessment and Water Research (IDAEA)
Spanish National Research Council (CSIC)
C/ Jordi Girona 18-26, 08034 Barcelona, Spain

Keywords: Viscoelastic-viscoplastic, time-dependency, strain-softening, creep-failure, delayed failure

Abstract. *An alternative Burgers-viscoplastic strain-softening (BVSS) constitutive model is proposed in this paper, to simulate the time-dependency, strain-softening and creep-failure behaviours of geomaterials. The proposed BVSS model incorporates the Burgers viscoelastic model combined with the viscoplastic model. Mohr-Coulomb and Hoek-Brown strain-softening models have been considered. The proposed BVSS constitutive model has been implemented into Finite Element Method software CODE_BRIGHT. A good agreement can be observed between the obtained numerical results and analytical solutions. After that, parametric analyses are carried out to investigate the creep-failure response. This study provides an alternative numerical approach to simulate the more actual behaviour of geomaterials.*

1. INTRODUCTION

Geomaterials undergo time-dependency and progressive damage evolution during the long-term period [1–3]. As shown in Figure 1, in creep tests of some types of rock samples, the deformation increases with time under a constant applied load. The creep deformations takes account for a large amount of the total displacements, which should be considered in representing more actual behaviour of geomaterials [4]. Furthermore, in a geomechanics framework, accidents are frequently related to fractures. The post-failure behaviour varies according to rock mass quality. Rock masses of different qualities may exhibit different post-failure behaviours, including perfectly plastic, strain-softening or brittle behaviours [5]. Therefore, post-failure behaviour should be considered in rock mechanics.

In many practical engineering projects, the actual behaviour of geomaterials is governed by both plastic and creep effects. Some underground structures show large delayed deformations that could lead to failure, *i.e.* creep-induced failure response, which may be relevant for many engineering cases, such as for some tunnels that do not fail during excavation but ultimately fail after a long-term operation. The delayed failure behaviour may cause by progressive damage coupled with creep behaviour. In this research, a Burgers-Viscoplastic strain-softening (BVSS) constitutive model is proposed to simulate the time-dependency, strain-softening and creep-failure behaviour of geomaterials.

2. METHODOLOGY

In the Burgers-Viscoplastic strain-softening (BVSS) constitutive model, the total strain rate tensor ($d\boldsymbol{\varepsilon}/dt$) can be decomposed into components describing the Maxwell ($d\boldsymbol{\varepsilon}_{\mathrm{M}}/dt$),

Kelvin ($d\boldsymbol{\varepsilon}_{\mathrm{K}}/dt$) and the viscoplastic ($d\boldsymbol{\varepsilon}_{\mathrm{vp}}/dt$) parts, as shown in Equation (1) [2]. Meanwhile, the Maxwell part can be decomposed into elastic spring ($d\boldsymbol{\varepsilon}_{\mathrm{M}}^{\mathrm{e}}/dt$) and viscous ($d\boldsymbol{\varepsilon}_{\mathrm{M}}^{\mathrm{v}}/dt$) parts.

$$\frac{d\boldsymbol{\varepsilon}}{dt}=\frac{d\boldsymbol{\varepsilon}_{\mathrm{M}}}{dt}+\frac{d\boldsymbol{\varepsilon}_{\mathrm{K}}}{dt}+\frac{d\boldsymbol{\varepsilon}_{\mathrm{VP}}}{dt}=\frac{d\boldsymbol{\varepsilon}_{\mathrm{M}}^{\mathrm{e}}}{dt}+\frac{d\boldsymbol{\varepsilon}_{\mathrm{M}}^{\mathrm{v}}}{dt}+\frac{d\boldsymbol{\varepsilon}_{\mathrm{K}}}{dt}+\frac{d\boldsymbol{\varepsilon}_{\mathrm{VP}}}{dt} \tag{1}$$

The strain rates corresponding to Maxwell, Kelvin and viscoplastic models can be expressed as in Equations (2)-(5), respectively. $\mathbf{D}_{\mathrm{i}}^{\mathrm{e}}$ (or $\mathbf{C}_{\mathrm{i}}^{\mathrm{e}}$) and $\mathbf{D}_{\mathrm{i}}^{\mathrm{v}}$ (or $\mathbf{C}_{\mathrm{i}}^{\mathrm{v}}$) represent the tangent stiffness matrices (or the compliance matrices) of the elastic spring and of the viscous dashpot in the i model (i = M or K represents the Maxwell model or the Kelvin model); η_{M} (or η_{K}) is the viscosity of the viscous dashpot in the Maxwell (or the Kelvin) model; η_{vp} is the viscosity of the viscoplastic model; F and G represent the overstress function and the viscoplastic potential, respectively, of the viscoplastic model [2].

$$\frac{d\boldsymbol{\varepsilon}_{\mathrm{M}}}{dt}=\frac{d\boldsymbol{\varepsilon}_{\mathrm{M}}^{\mathrm{e}}}{dt}+\frac{d\boldsymbol{\varepsilon}_{\mathrm{M}}^{\mathrm{v}}}{dt}=\mathbf{C}_{\mathrm{M}}^{\mathrm{e}}\frac{d\boldsymbol{\sigma}'}{dt}+\frac{\boldsymbol{\sigma}'}{\eta_{\mathrm{M}}}=\left(\mathbf{D}_{\mathrm{M}}^{\mathrm{e}}\right)^{-1}\frac{d\boldsymbol{\sigma}'}{dt}+\frac{\boldsymbol{\sigma}'}{\eta_{\mathrm{M}}} \tag{2}$$

$$\frac{d\boldsymbol{\varepsilon}_{\mathrm{K}}}{dt}=\mathbf{C}_{\mathrm{K}}^{\mathrm{v}}(\boldsymbol{\sigma}'-\boldsymbol{\varepsilon}_{\mathrm{K}})=\left(\mathbf{D}_{\mathrm{K}}^{\mathrm{v}}\right)^{-1}(\boldsymbol{\sigma}'-\boldsymbol{\varepsilon}_{\mathrm{K}}) \tag{3}$$

$$\frac{d\boldsymbol{\varepsilon}_{\mathrm{vp}}}{dt}=\frac{1}{\eta_{\mathrm{vp}}}\langle\Phi(F)\rangle\frac{\partial G}{\partial\boldsymbol{\sigma}'} \tag{4}$$

$$<\Phi(F)>=\begin{cases}\Phi(F) & \text{if } \Phi(F)\geq 0\\ 0 & \text{if } \Phi(F)<0\end{cases} \tag{5}$$

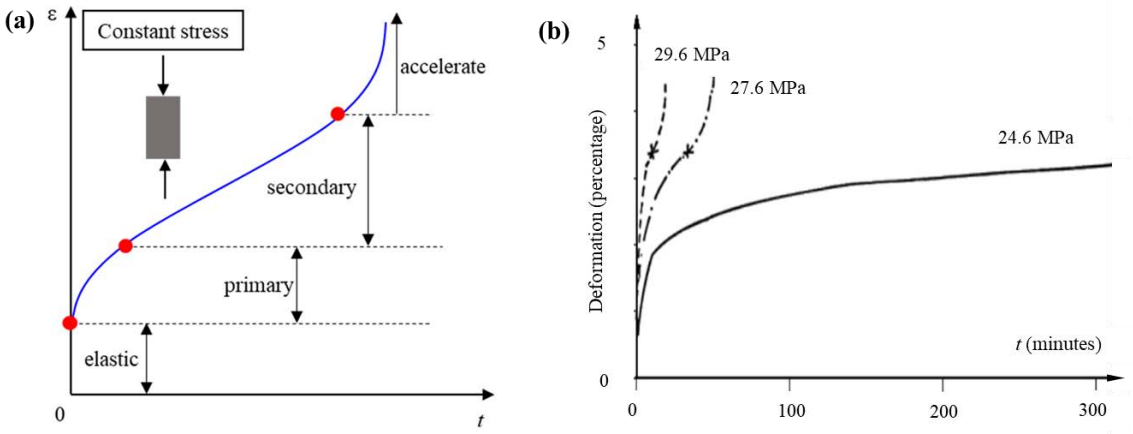

Figure 1. (a) Creep curves of soft rock samples (conceptual model), and **(b)** Creep curves of halite samples. Based on the work of [2,6].

The expression of the Mohr-Coulomb and Hoek-Brwon strain-softening failure criteria are presented in Equations (6) and (7), respectively. The Mohr-Coulomb form of the potential has been implemented in CODE_BRIGHT, which can express in Equation (8). c(η) and φ(η) are the plastic strain-dependent cohesion and the friction angle, respectively. $m_{\mathrm{HB}}(\eta)$ and $s_{\mathrm{HB}}(\eta)$

are the plastic strain-dependent parameters of the Hoek-Brown failure criterion and σ_{ci} is the uniaxial compressive strength of the intact rock. $\psi(\eta)$ is the dilatancy angle. p, J_2 and θ represent the mean stress, the second invariable stress, and the lode angle, respectively. Moreover, the softening parameter η is defined as shown in Equation (9).

$$F_{MC} = p\sin\varphi(\eta) + \sqrt{J_2}\left(\cos\theta - \frac{1}{\sqrt{3}}\cdot\sin\varphi(\eta)\cdot\sin\theta\right) - c(\eta)\cos\varphi(\eta) \tag{6}$$

$$F_{HB} = \left[\frac{4}{\sigma_{ci}}\cos^2\theta\sqrt{J_2} + \frac{2}{\sqrt{3}}m_{HB}(\eta)\cos\left(\theta + \frac{\pi}{6}\right)\right]\sqrt{J_2} - m_{HB}(\eta)\left[-p + \frac{s_{HB}(\eta)\sigma_{ci}}{m_{HB}(\eta)}\right] \tag{7}$$

$$G = p\sin\psi(\eta) + \sqrt{J_2}\left(\cos\theta - \frac{1}{\sqrt{3}}\sin\psi(\eta)\sin\theta\right) \tag{8}$$

$$\eta = \sqrt{\frac{3}{2}\left[\left(\varepsilon_x^p - \varepsilon_m^p\right)^2 + \left(\varepsilon_y^p - \varepsilon_m^p\right)^2 + \left(\varepsilon_z^p - \varepsilon_m^p\right)^2 + \left(\frac{1}{2}\gamma_{xy}^p\right)^2 + \left(\frac{1}{2}\gamma_{yz}^p\right)^2 + \left(\frac{1}{2}\gamma_{zx}^p\right)^2\right]} \tag{9}$$

A linearly decreasing function of plastic parameters $k(\eta)$ is adopted to represent the damage evolution, as shown in Equation (10), where k_{peak} and k_{res} are the peak and residual values of k, respectively. When adopting the Mohr-Coulomb failure surface, k represents the cohesion c and friction angle φ, while k represents the m_{HB} and s_{HB} parameters when considering the Hoek-Brown failure surface. In future research, a non-linear function will be introduced to describe the evolution of strength parameters.

$$k(\eta) = \begin{cases} k_{peak}, & \text{for } \eta < 0 \\ k_{peak} + \left(\dfrac{k_{res} - k_{peak}}{\eta^*}\right)\eta, & \text{for } 0 \le \eta < \eta^* \\ k_{res}, & \text{for } \eta \ge \eta^* \end{cases} \tag{10}$$

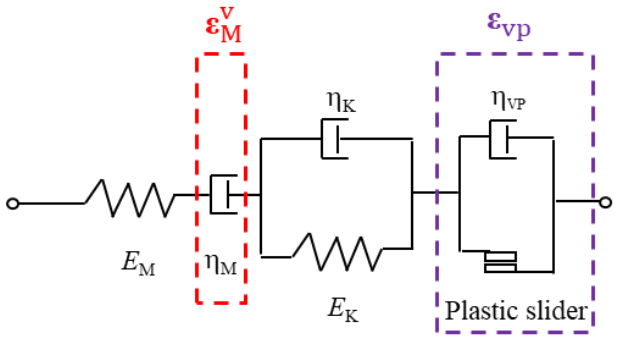

Figure 2. The conceptual model of the Burgers-Viscoplastic strain-softening constitutive model. Based on the work of Song [2] and Song et al. [3]

In the proposed BVSS model, the progressive damage coupled with creep behaviour to simulate failure induced by creep and the subsequent progressive damage. In other words, the unrecoverable strain of the BVSS model is the sum of the viscous part of the Maxwell model ($\boldsymbol{\varepsilon}_{\mathrm{M}}^{\mathrm{v}}$) and the viscoplastic part ($\boldsymbol{\varepsilon}_{\mathrm{vp}}$). Both strains ($\boldsymbol{\varepsilon}_{\mathrm{M}}^{\mathrm{v}}$ and $\boldsymbol{\varepsilon}_{\mathrm{vp}}$) are accumulated to account for softening process. Then, the proposed BVSS model can be used to simulate the coupled behaviour between creep deformation and damage evolution, and thus, to represent the creep-failure (or named delayed failure) behaviour of geomaterials [2].

3. NUMERICAL VERIFICATION

A creep test is made here to verify the numerical implementation of the Burgers viscoelastic model. In the numerical simulation, from time t = 0 to t = t_1, the applied stress is σ_0; then, the applied stress is changed from σ_0 to σ_1 at the moment of t = t_1. The analytical solutions of strain for the creep tests can express in Eq. (11).

$$\varepsilon(t)=\begin{cases}\dfrac{\sigma_0}{E_{\mathrm{K}}}\left(1-e^{-\frac{t}{\eta_{\mathrm{K}}/E_{\mathrm{K}}}}\right)+\dfrac{\sigma_0}{E_{\mathrm{M}}}+\dfrac{\sigma_0}{\eta_{\mathrm{M}}}t, 0\le t\le t_1 \\ \dfrac{\sigma_0}{E_{\mathrm{K}}}\left(1-e^{-\frac{t}{\eta_{\mathrm{K}}/E_{\mathrm{K}}}}\right)-\dfrac{\sigma_0}{E_{\mathrm{K}}}\left(1-e^{-\frac{t-t_1}{\eta_{\mathrm{K}}/E_{\mathrm{K}}}}\right)+\dfrac{\sigma_1}{E_{\mathrm{K}}}\left(1-e^{-\frac{(t-t_1)}{\eta_{\mathrm{K}}/E_{\mathrm{K}}}}\right)+\dfrac{\sigma_1}{E_{\mathrm{M}}}+\dfrac{\sigma_0}{\eta_{\mathrm{M}}}t_1+\dfrac{\sigma_1}{\eta_{\mathrm{M}}}(t-t_1), t\ge t_1\end{cases} \tag{11}$$

In the comparison, the input parameters are: t_1 = 50 day, η_{M} = 50000 MPa day, E_{M} = 2000 MPa, η_{K} = 10000 MPa day, E_{K} = 1000 MPa, ν = 0.499, σ_0 = 20 MPa, σ_1 = 50 MPa. Figure 3 presents the numerical model in CODE_BRIGHT simulations. Figure 4 presents the comparison of strains between the analytical solutions and CODE_BRIGHT results. A good agreement between CODE_BRIGHT results and analytical solutions can be observed, which can verify the obtaiend numericla results in CODE_BRIGHT.

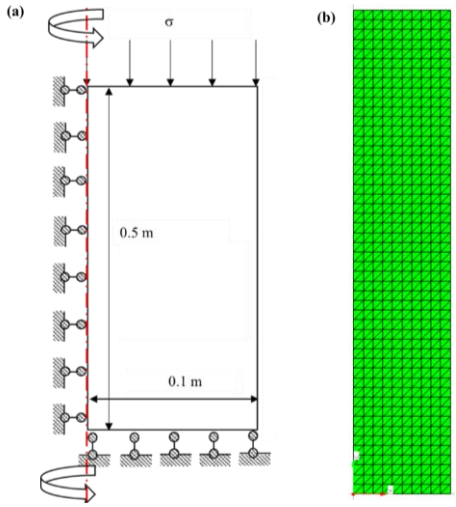

Figure 3. Creep numerical test: **(a)** basic features and boundary conditions (not real scale), and **(b)** mesh size (1000 triangle quadratic elements).

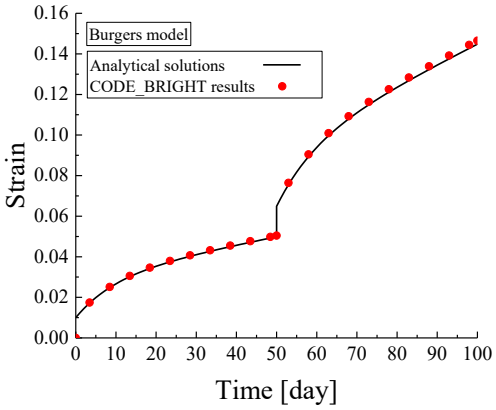

Figure 4. Comparison of strain between the analytical solutions and CODE_BRIGHT results for a creep test.

4. CREEP-FAILURE BEHAVIOUR

Numerical analyses of creep-failure behaviour are presented in this suction, based on the work presented in Song [2]. Creep tests are carried out to analyse the creep-induced failure behaviour of the proposed BVSS model. Three different constitutive models are used in this section, including the Burgers viscoelastic model, the Burgers-viscoplastic perfectly-plastic (BVPP) model and the Burgers-viscoplastic strain-softening (BVSS) model. The numerical model is 2D axisymmetric with dimensions of 0.01 m × 0.05 m. The normal displacements along the bottom and left boundaries have been restrained. A mesh with 2250 quadratic triangle elements has been considered for the analysis. In the numerical simulations, at time t = 0, a constant stress p_y is applied along the top boundary. The calculation is stopped at 150 days. The rock mass is considered incompressive, and the input parameters are shown in Table 1. No dilatancy is considered in the perfectly plastic behaviour model.

As shown in Figure 5. In the case of the BVSS model, the resulting strain is the same as that of Burgers at the start of the simulation –*i.e.* when there is only a viscoelastic response–. However, as the accumulated unrecoverable strain increases, the yield surface decreases due to softening induced by creep. Consequently, when the yield surface reaches the point of our analysis, the strain rate accelerates due to both the creep and viscoplastic contributions. Based on the presented results in Figure 5, it can conclude that the proposed BVSS model can simulate the creep-failure behaviour of geomaterials.

Table 1. Input parameters for the uniaxial creep tests [2,3].

Viscoelastic model	Maxwell model	E_M	6000 MPa	η_M	7.776×10^9 MPa.s
	Kelvin model	E_K	3000 MPa	η_K	1.296×10^9 MPa.s
Viscoplastic model	Cohesion	c_{peak}	10 MPa	c_{res}	5 MPa
	Friction angle	φ_{peak}	50 deg	φ_{res}	20 deg
	Dilatancy	α	1	$\psi_{peak} = \psi_{res}$	5 deg
	Perzyna model	m	5	η_{vp}	10^{10} MPa^{m}s

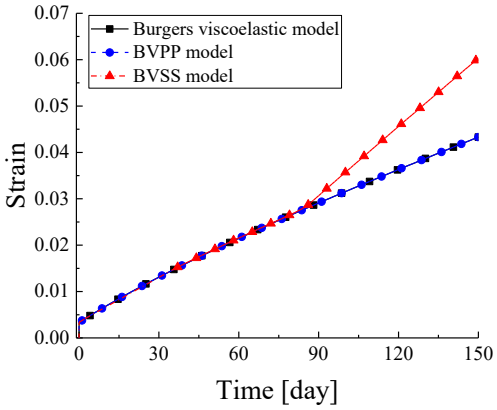

Figure 5. Axial strains versus time, comparison between Burgers, BVPP and BVSS models [2,3].

5. CONCLUSIONS

The Burgers-Viscoplastic strain-softening (BVSS) constitutive model has been proposed and implemented in the Finite Element Method software CODE_BRIGHT. In the proposed BVSS model, the Burgers viscoelastic model is combined with the strain-softening post-failure behaviour model. As a verification step, a good agreement between CODE_BRIGHT results and analytical solutions has been observed. Due to the coupled behaviour between damage evolution and creep response, this model can simulate the primary and secondary creep responses and the creep-failure behaviour of geomaterials.

ACKNOWLEDGEMENTS

This research was supported by the CODE_BRIGHT Project (International Centre for Numerical Methods in Engineering). Fei Song was supported by a CSC scholarship (No. 201706260240).

REFERENCES

[1] Song F, Rodriguez-Dono A, Olivella S, Zhong Z. Analysis and modelling of longitudinal deformation profiles of tunnels excavated in strain-softening time-dependent rock masses. Comput Geotech 2020;125:103643.

[2] Song F. Modelling time-dependent plastic behaviour of geomaterials. Universitat Politècnica de Catalunya (UPC), Ph.D. thesis, 2021.

[3] Song F, Rodriguez-Dono A, Olivella S, Gens A. Coupled solid-fluid response of deep tunnels excavated in saturated rock masses with a time-dependent plastic behaviour. Appl Math Model 2021.

[4] Wang HN, Li Y, Ni Q, Utili S, Jiang MJ, Liu F. Analytical solutions for the construction of deeply buried circular tunnels with two liners in rheological rock. Rock Mech Rock Eng 2013;46:1481–98.

[5] Rodriguez-Dono A. Studies on undergrond excavations in rock masses. Universidade de Vigo, Ph.D. thesis, 2011.

[6] Ramírez Oyanguren P. A study of longwall mining in potash. University of Newcastle, 1966.

COMPARISON OF LABORATORY TESTS SIMULATIONS WITH CODE_BRIGHT IN SMALL AND LARGE STRAIN SETTINGS WITH ANALYTICAL SOLUTIONS

X. Pintado[(1)], J. Alcoverro[(2)]

[(1)]AINS Group; Bertel Jungin aukio 9, 02600 Espoo, Finland
Email: xavier.pintado@ains.fi
[(2)]Department of Civil and Environmental Engineering, Universitat Politècnica de Catalunya, Barcelona, Spain

Key words: codes verification; simple shear test; triaxial test; large strains.

Abstract. *Verification is an important exercise for assuring the quality of computer codes and for detecting mistakes during their preparation. This work compares some analytical solutions that reproduce shear laboratory tests in small strains setting, in updated mesh (Lagrangian option) and formulations in large strains with objective rates with the results obtained with CODE_BRIGHT. The tests are the simple shear test and the drained triaxial test at constant lateral confining pressure.*

1 INTRODUCTION

The spent nuclear fuel generated in nuclear power plants should be stored in repositories which must be stable during thousands of years. The storage in deep geological disposals is one option considered in many countries. Finland and Sweden have developed a geological disposal method called KBS-3[1,2] which involves the excavation of a network of tunnels in crystalline rock at 400-500 m depth in order to store the spent nuclear fuel in metal containers surrounded by a clay barrier constructed with compacted bentonite.

Although the Finnish repository will be constructed far from active plate margins (Posiva, 2013), the possibility of large earthquakes, especially at the time of ice-sheet retreat, cannot be totally excluded[2,3].

For the assessment of the bentonite behaviour against shear loads, it is possible to do different shear tests like the simple shear test[4] or the triaxial tests with constant shear rate[5] or with constant load rate (Bishop-Wesley triaxial cell[6]). These tests can be simulated with computer codes in order to calibrate the constitutive models that are used for the simulation of the clay barrier. Different models can be used for assessing the clay barrier, like the von Mises model with hardening[7] used for the metal container design or the BBM model[8], which has been used by Åkesson et al.[9] and Toprak et al.[10] for the simulation of the clay barrier hydration and swelling pressure development.

A way to extend FEM codes in the small strains setting to a large strains setting involves the use of mesh updating and of a particular rate of stress variables in the small strains rate constitutive equations: material derivative (CODE_BRIGHT), Jaumann rate (Abaqus) or Hill rate (Plaxis). Note that only in the last two cases, the obtained large strains constitutive equations are frame indifferent. It is necessary to verify that these models are correctly implemented. To do that, it is possible to compare the results provided by the code assessed with other codes already verified but it is also possible to verify the codes comparing the results with the results provided by analytical solutions.

The analytical solutions of the simple shear test and triaxial test considering the von Mises model without hardening (similar to model used by Jonsson et al.[7] in canister design) and the Modified Cam

clay model (equivalent to BBM in saturated conditions) have been obtained[11] and were used for the models' verification.

2 SIMULATION OF THE SIMPLE SHEAR TEST

Simple shear test is widely used in soil mechanics. The basis of this test is shown in Figure 1a. More information about the test procedure and the test set-up description can be found in ASTM[12].

The test is simulated with a monotonic increase of the horizontal displacements on the top of the sample (Figure 1b).

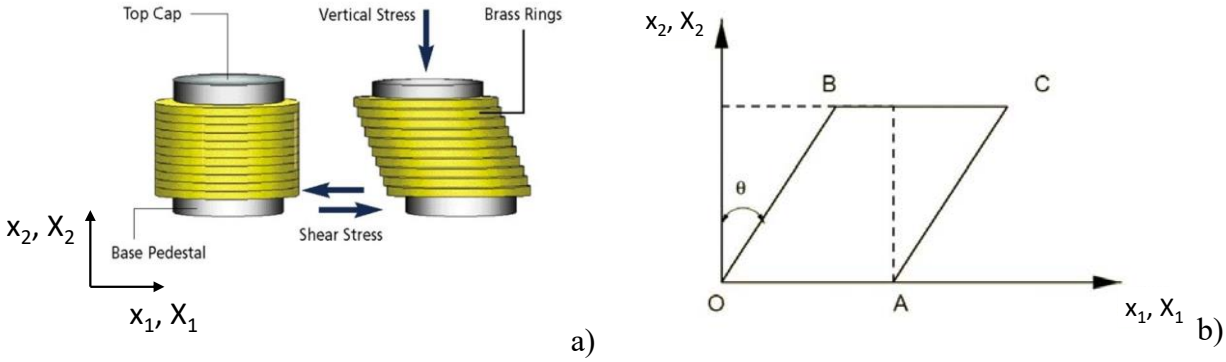

Figure 1. a) Basis of the simple shear test. b) Simple shear test modelling. (from Ji[13]).

The results obtained by CODE_BRIGHT were compared with the analytical solutions obtained using small strains setting, one of the large strains setting implemented in Abaqus (Jaumann rate[14]) and the updated mesh setting (Lagrangian method) used in CODE_BRIGHT[15].

Figure 2 presents the comparation between CODE_BRIGHT results and the analytical solutions when the constitutive model was the von Mises.

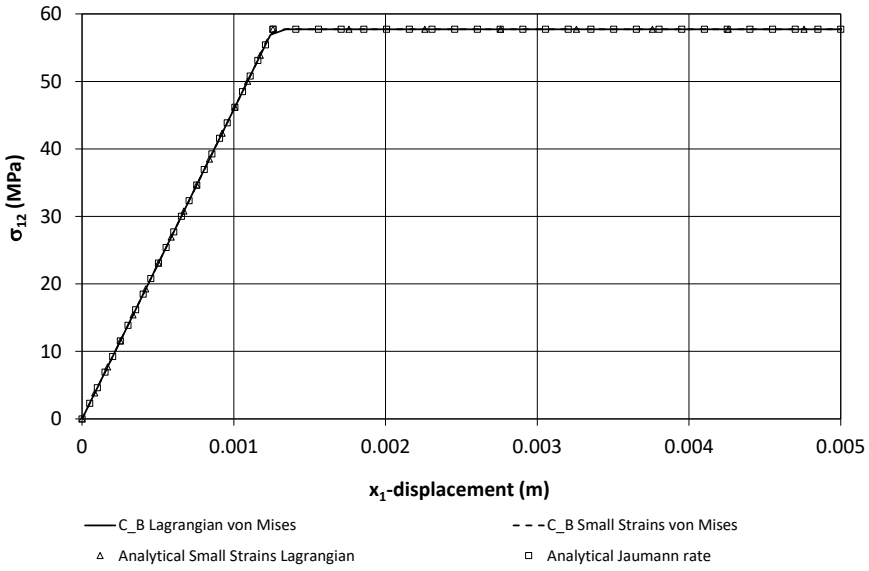

Figure 2. CODE_BRIGHT results and analytical solutions. Von Mises model. Dimensions of the sample: 1×1 m.

Figure 3 presents the comparation between CODE_BRIGHT results and the analytical solutions when the constitutive model was the Modified Cam clay.

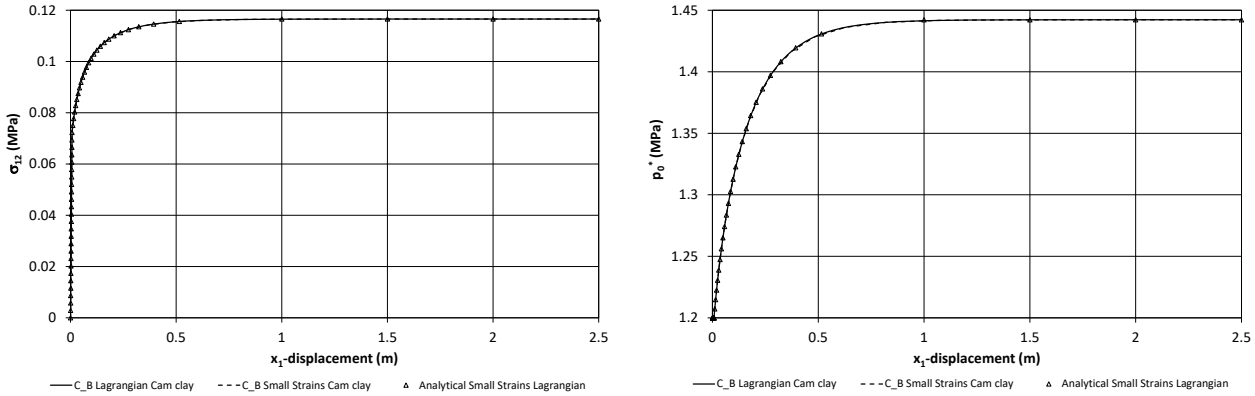

Figure 3. CODE_BRIGHT results and analytical solutions. Modified Cam clay model. Shear stress vs axial displacement (left) and p_0^* vs axial displacement (right). Dimensions of the sample: 1×1 m.

3 SIMULATION OF THE TRIAXIAL TEST

Triaxial test is also widely used in soil mechanics. The basis of this test is shown in Figure 4a. More information about the test procedure and the test set-up description can be found in ASTM[16].

The test is simulated with a monotonic increase of the vertical displacements on the top of the sample at constant lateral confining pressure (σ_r) in drained conditions (Figure 4b).

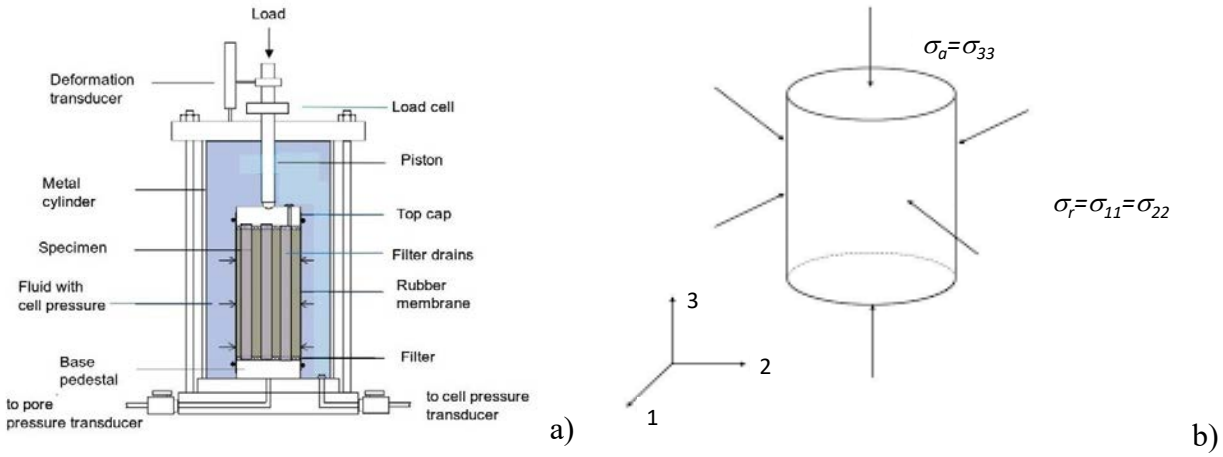

Figure 4. a) Basis of the triaxial test[17]. b) Triaxial test modelling (right).

The results obtained by CODE_BRIGHT were compared with the analytical solutions obtained using small strains setting, the large strains setting used in PLAXIS (Hill rate[18]; only in von Mises model), Abaqus (Jaumann rate[14]) and the updated mesh setting (Lagrangian method) used in CODE_BRIGHT[15].

Figure 5 presents the comparation between CODE_BRIGHT results and the analytical solutions when the constitutive model was the von Mises.

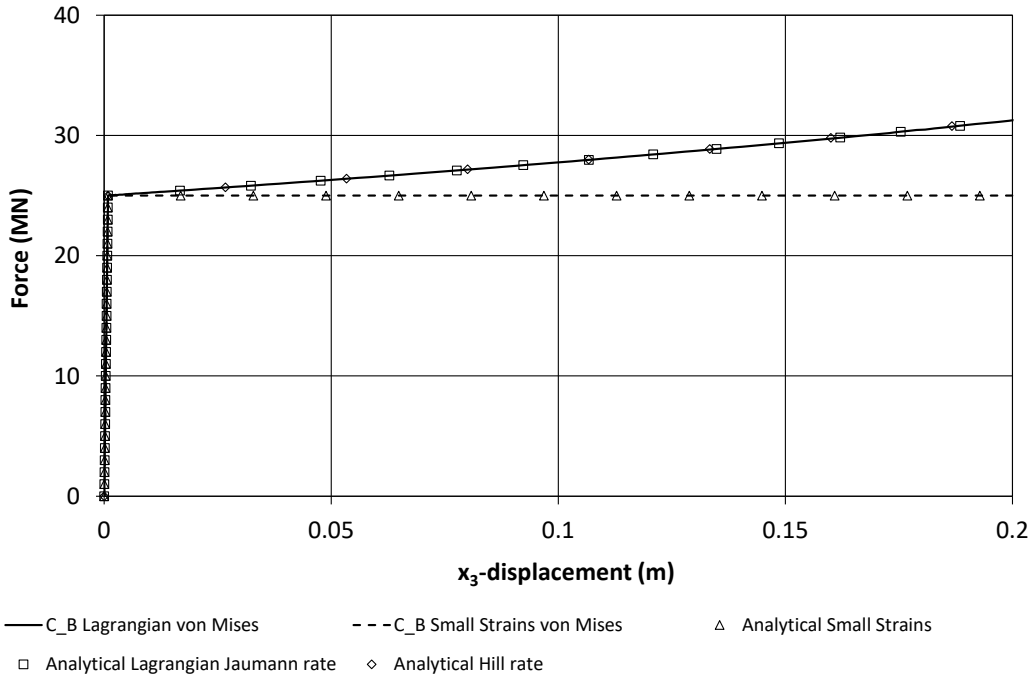

Figure 5. CODE_BRIGHT results and analytical solutions. Von Mises model. Dimensions of the sample: 0.5×0.5×1 m.

Figure 6 presents the comparation between CODE_BRIGHT results and the analytical solutions when the constitutive model was the Modified Cam clay.

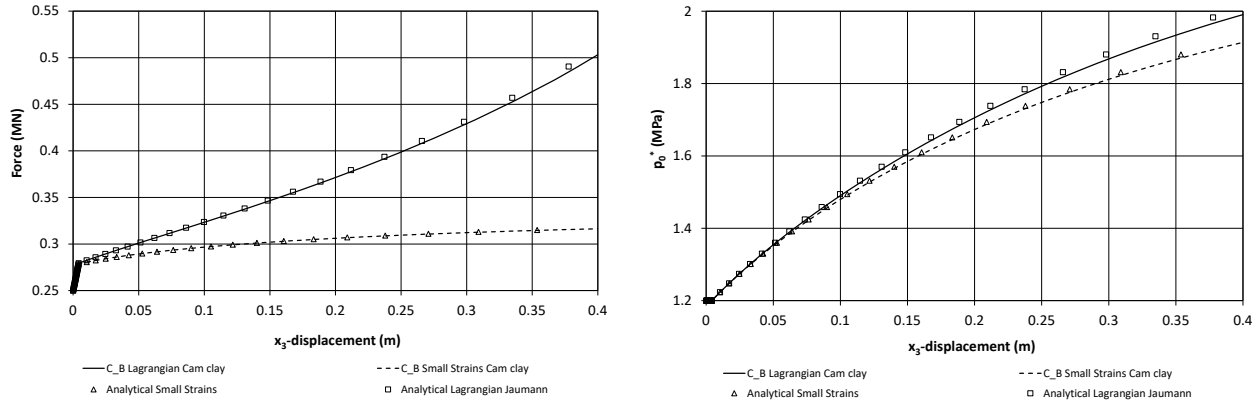

Figure 6. CODE_BRIGHT results and analytical solutions. Modified Cam clay model. Axial force vs axial displacement (left) and p_0^* vs axial displacement (right). Dimensions of the sample: 0.5×0.5×1 m.

4 CONCLUSIONS

- The comparation of the CODE_BRIGHT results with the analytical solutions obtained from the simulations of the simple shear test and triaxial test using the von Mises and the Modified Cam clay models verify the computer code for these simple geometries and load paths.
- The verification exercise should continue comparing the results obtained in CODE_BRIGHT with the results obtained in other computer codes in more complex geometries and load paths without analytical solution.

ACKNOWLEDGEMENTS

This work was supported by Posiva Oy and AINS Group.

REFERENCES

[1] SKB, 2010. Design, production and initial state of the closure. SKB Technical report TR-10-17, Stockholm, Sweden.

[2] Posiva, 2013. Safety case for the disposal of spent nuclear fuel at Olkiluoto. Performance assessment 2012. Posiva Report 2012-04. Eurajoki, Finland.

[3] Saari, J., 2012. Seismic activity parameters of the Olkiluoto site. Posiva Report 2012-34. Eurajoki. Finland

[4] Bjerrum, L., Landva, A., 1966. Direct simple shear tests on a Norwegian quick clay. Géotechnique 16(1), 1-20.

[5] Bishop, A.W., Henkel, D.J. (1962). The measruement of soil properties in the triaxial test. Ed. Arnold. London, United Kingdom.

[6] Bishop, A.W., Wesley, L.D. (1975). A hydraulic triaxial cell aparatus for controlled stress path testing. Géotechnique 25(4): 657-670.

[7] Jonsson, M., Emilsson, G., Emilsson, L., 2018. Mechanical design analysis for the canister. Posiva SKB report 04. Eurajoki, Finland.

[8] Alonso, E.E., Gens, A., Josa, A., 1990. A constitutive model for partially saturated soils. Géotechnique 40(3), 405-430.

[9] Åkesson, M., Börgesson, L., Kristensson, O. (2010). SR Site data report. THM modelling of buffer, backfill and other system components. Updated 2013-12. SKB report TR-10-44. Stockholm, Sweden.

[10] Toprak, E., Olivella, S. Pintado, X. (2018). Modelling engineered barriers for spent nuclear fuel repository using a double structure approach for pellet based components. Journal of Environmental Geotechnics 7(1): 72-94.

[11] Pintado, X., Kuutti, J., Alcoverro, J. (2021). Modelling of simple shear and triaxial tests. Eurajoki, Finland: Posiva Oy. Technical Memorandum, kronodoc: POS-032369.

[12] ASTM D6528 - 17 Standard Test Method for Consolidated Undrained Direct Simple Shear Testing of Fine Grain Soils, ASTM International, West Conshohocken, PA, www.astm.org

[13] Ji, W., Waas, A. M., Bazant, Z. P. 2013. On the importance of work-conjugacy and objective stress rates in finite deformation incremental finite element analysis. Journal of Applied Mechanics, Transactions ASME, 80(4), [041024].

[14] Dassault Systèmes (2011). Abaqus 6.11. Analysis User's Manual. Dassault Systèmes Simulia Corp., Providence, RI, USA.

[15] DECA-UPC. (2020). CODE_BRIGHT User's guide. Department of Civil and Environmental Engineering, Escola de Camins. Universitat Politècnica de Catalunya, Barcelona, Spain.

[16] ASTM D7181-20.2020. Standard Test Methods for Consolidated Drained Triaxial Compression Test for Soils, ASTM International, West Conshohocken, PA, www.astm.org

[17] Dueck, A, Börgesson, L, Johannesson, L.-E. 2010. Stress-strain relation of bentonite at undrained shear. Laboratory tests to investigate the influence of material composition and test technique. SKB technical report TR-10-32. Stockholm. Sweden.

[18] van Langen, H. (1991). Numerical Analysis of Soil-Structure Interaction. Ph.D. thesis. Technische Universiteit Delft, the Netherlands.

VERIFICATION OF AN ANALYTICAL SOLUTION FOR POROELASTIC STRESS CHANGES DUE TO RESERVOIR PRESSURIZATION/DEPLETION

Haiqing Wu [*,†], Victor Vilarrasa [††], Silvia De Simone [†††], Maarten W. Saaltink [†] and Francesco Parisio [††]

[†] Department of Civil and Environmental Engineering, Universitat Politécnica de Catalunya (UPC),
Associated Unit: Hydrogeology Group (UPC-CSIC)
Jordi Girona 1-3, 08034 Barcelona, Spain

[††] Institute of Environmental Assessment and Water Research (IDAEA), CSIC,
Associated Unit: Hydrogeology Group (UPC-CSIC)
c/ Jordi Girona 18, 08034 Barcelona, Spain

[†††] Univ Rennes, CNRS, Géosciences Rennes - UMR 6118, 35000 Rennes, France

[*] Corresponding autor e-mail: haiqing.wu@upc.edu

Key words: Reservoir pressurization/depletion; inclusion theory; permeable and impermeable faults; poroelastic stress

Abstract. *Understanding poromechanical response to injection/pumping into subsurface formations is crucial to assess the potential risk of induced seismicity. Analytical solutions facilitate the parametric space analysis of complex problems involved in geo-energy and geo-engineering applications. Yet, as the complexity of the problems increases, it becomes necessary to verify the analytical solutions against numerical ones. Here, we verify an analytical solution to poroelastic stress changes induced by pressurization/depletion of a reservoir intersected by a fault that can be either permeable or impermeable. In particular, we evaluate the poroelastic stress changes in a pressurized reservoir and its surrounding, focusing on the displaced fault, and we make a detailed comparison between results from our analytical solution and numerical simulations with CODE_BRIGHT. The comparison shows that the analytical results are in good agreement with the numerical ones, which confirms the accuracy and correctness of the analytical solution. The proposed solution represents a valid and useful tool in geo-energy related projects.*

1 INTRODUCTION

Geo-energy and environment related activities involve deep injecting or pumping of fluids: geothermal energy production and geologic carbon storage are essential technologies to reach zero or negative net carbon emissions; natural gas storage is an effective strategy to adjust the seasonal imbalance of energy demand; disposal of wastewater is an indispensable approach to mitigate environmental deterioration. By altering the in-situ stress field, this fluid injection/production may lead to fault reactivation and induced seismicity[i]. Therefore, an accurate estimate of the fluid-induced poroelastic stress changes is key. Poroelastic stress in general is much larger within the reservoir and in its vicinity than in the surrounding rocks. The presence of a fault crossing the reservoir results in an additional stress concentration, especially when the fault offsets the reservoir[ii]. A relevant example is the Groningen gas field, where a series of studies have identified the presence of permeable faults in the reservoir[iii]. In

the majority of stratified sedimentary basins, clay smearing is likely to reduce fault permeability[iv]. As a result, the fault generally presents a low permeability such that it can be considered as impermeable, like in the case of low-permeable faults detected in Snohvit field[v] and Pohang[vi]. Understanding the poromechanical responses in the presence of both permeable and impermeable displaced faults is particularly relevant to minimize the induced seismicity risk.

Analytical solutions represent a fast and efficient tool to perform the parametric space analysis of complex problems. Yet, as the complexity of the solved problems increases, it becomes necessary to verify the analytical solutions against numerical ones. To this end, we here verify an analytical solution to poroelastic stress changes due to pressurization/depletion of a reservoir intersected by a displaced fault that could be either permeable or impermeable[vii], using the fully coupled finite element simulator CODE_BRIGHT[viii, ix].

2 METHOD

We derive the analytical solution for poroelastic stress changes σ_{ij} arising in a deep pressurized/depleted reservoir crossed by a displaced fault through the inclusion theory[vii, x]

$$\sigma_{ij}(x,y) = \frac{(1-2\nu)\alpha\Delta p}{2\pi(1-\nu)}\left[G_{ij}(x,y) - \pi\delta_{ij}\delta_{\Omega}\right], \tag{1}$$

where Ω is the inclusion domain, G_{ij} represents the surface integral of Green's function for stress, x and y are the Cartesian coordinates, α is Biot's coefficient, ν is the Poisson ratio, Δp is the pore pressure change, δ_{ij} is the Kronecker delta, and δ_{Ω} is the modified Kronecker delta. Negative stress denotes compression. The difference between permeable and impermeable faults resides in the surface integral G_{ij}. For the former case, pore pressure changes on both sides of the fault within the reservoir, while it only changes on the side of the fault where injection or depletion takes place for the latter case[vii].

As an example, we consider a 300-m thick reservoir with an infinite lateral extent (Figure 1). The reservoir and its surroundings are crossed by an inclined fault that could be either permeable or impermeable. In the numerical simulations, the impermeable surrounding rocks and fault are modeled by setting the intrinsic permeability to 10^{-18} m^2. A zero normal displacement is assigned to the lateral and lower boundaries. An overburden of -70 MPa, a value approximately representing a depth of 3.5 km, is imposed to the upper boundary. The initial stress state is isotropic; its magnitude is irrelevant but consistent with the assigned boundary condition. We adopt a linear elastic rock behavior, and a pressure buildup of 20 MPa in the entire reservoir for the permeable case. We take the scenario of injection into the left-hand side of the fault as an example of an impermeable case where the reservoir is compartmentalized. We consider the problem as two-dimensional and we include a surrounding geometry of 2 x 2 km to minimize boundary effects (Figure 1).

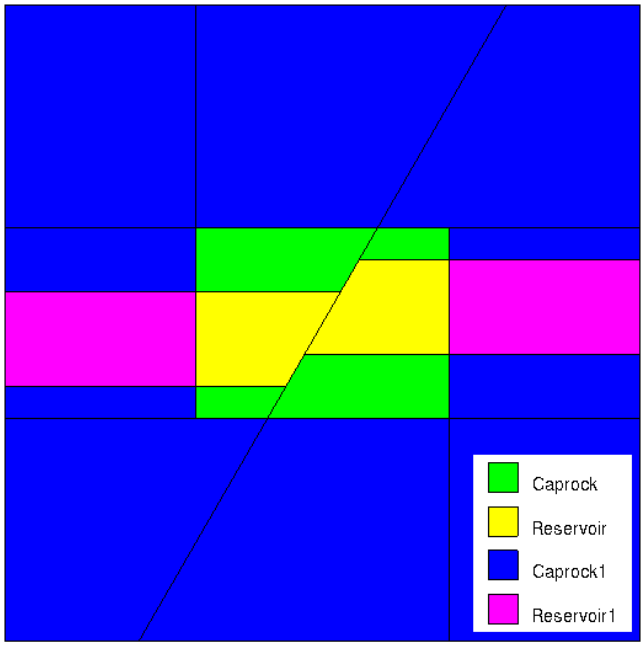

Figure 1: Geometrical domain and materials of the numerical simulations. For the purpose of demonstration in the post-process, the reservoir and its surrounding rocks are divided into several blocks with different material names, but with the same properties. Thus, the materials Reservoir and Reservoir 1 have the same material properties, and the properties of surrounding rock are assigned to the materials Caprock and Caprock 1.

3 RESULTS

For the purpose of verification, we compare the analytically evaluated poroelastic stress changes with the numerical results of CODE_BRIGHT. We first present a detailed comparison of the horizontal poroelastic stress changes for both the cases of a permeable (Figure 2) and impermeable (Figure 3) fault. We plot both the analytical and numerical results focusing on a rectangle of 800 m by 600 m centered in the fault, which corresponds to the center region (green and yellow blocks) shown in Figure 1. Figures 2 and 3 show that the analytical results are very similar to the numerical ones. The maximum and minimum of the poroelastic stress changes are always located in the corners between the reservoir and its surroundings due to stress concentration.

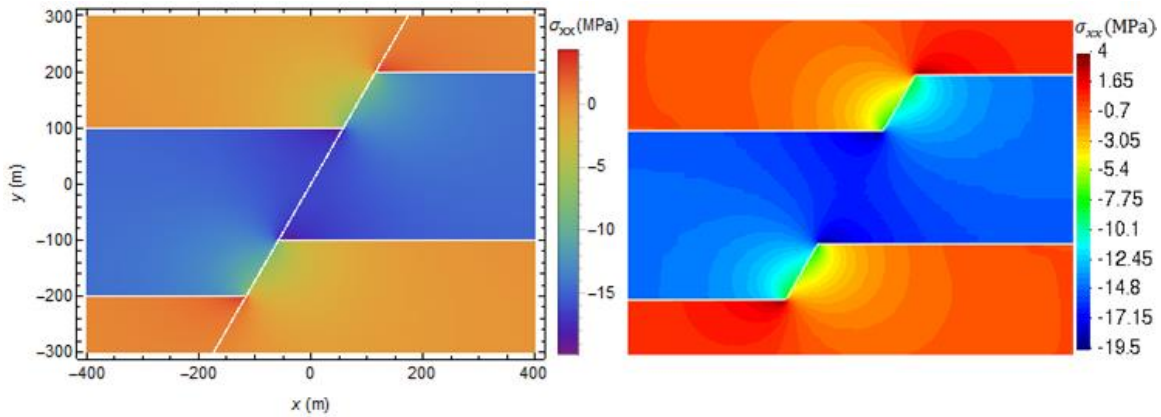

Figure 2: Horizontal poroelastic stress changes around a permeable fault evaluated by means of the analytical solution (left) and the numerical simulator CODE_BRIGHT (right) (adapted from Wu et al.[vii]).

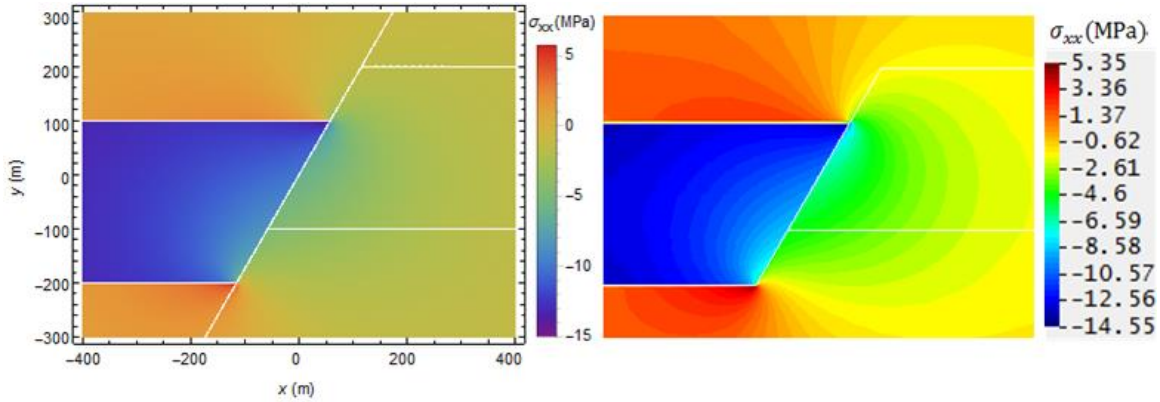

Figure 3: Horizontal poroelastic stress changes around an impermeable fault evaluated by means of the analytical solution (left) and the numerical simulator CODE_BRIGHT (right) (adapted from Wu et al.[vii]).

We then compare the numerically and analytically evaluated induced horizontal, vertical and *x*-*y* planar shear stress components along the fault plane for both permeable and impermeable cases (Figure 4). The results exhibit a good agreement for an arbitrary stress component, with only small discrepancies near the corners. The discrepancies are caused by the facts that: i) the analytical solution predicts singularities at corners that result in an infinite stress, whereas the numerical solution predicts finite values; ii) the sharp gradients at the corner are difficult to capture by the numerical solution because of its discrete resolution.

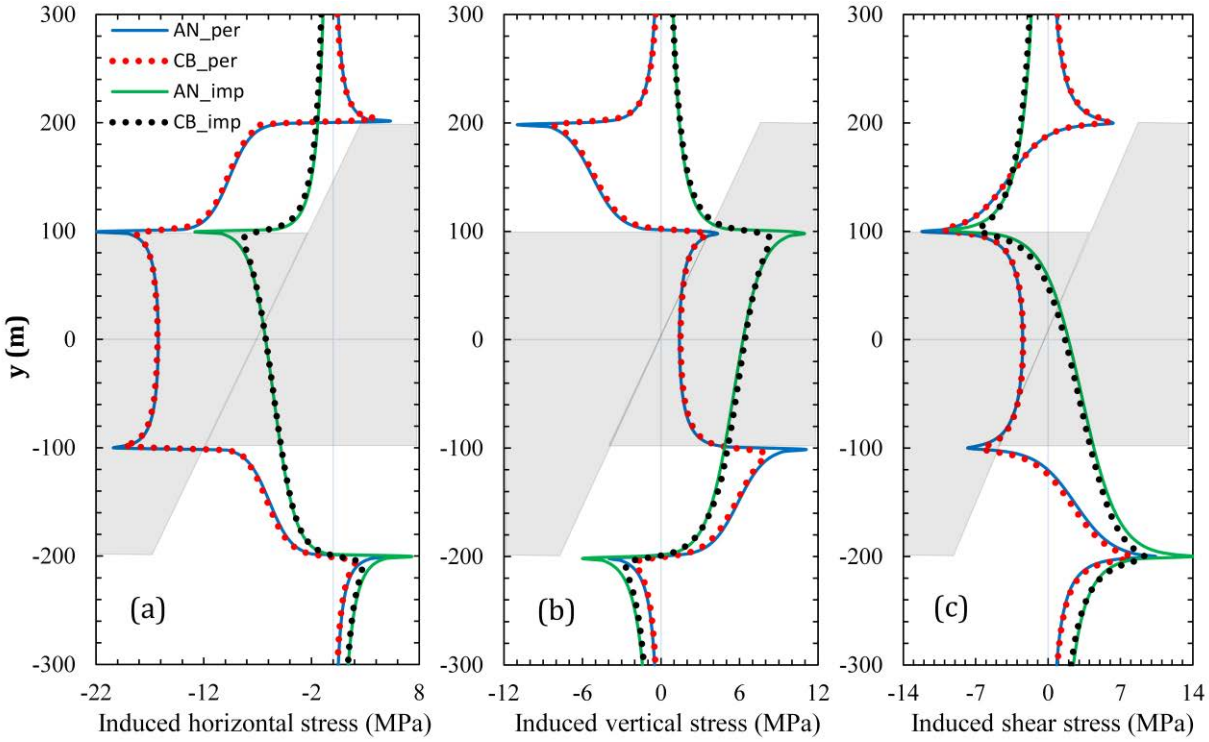

Figure 4: Comparison between analytically and numerically evaluated induced (a) horizontal, (b) vertical and (c) *x*-*y* planar shear stress components along the fault plane. Results along the fault are projected on the vertical axes *y*. The legend is shown in (a), indicating that solid lines represent the analytical results (AN) and dotted lines represent the numerical results from CODE_BRIGHT (CB), for both a permeable (per) and an impermeable (imp) fault. A schematic of the reservoir geometry is indicated by the grey background (adapted from Wu et al.[vii]).

The comparisons confirm the accuracy and correctness of the analytical solution (Figures 2-4), which is suitable for fault stability analysis and for the assessment of fault slip potential[vii]. Since the analytical solution is fast and efficient in parametric space analysis, it could be a powerful tool for risk assessment of induced seismicity, site selection, and supporting decision making during the lifetime of geo-energy projects.

4 CONCLUSIONS

We have made a detailed comparison between analytical and numerical solutions of poroelastic stress changes within a pressurized reservoir and its surrounding rock, which are displaced by either a permeable or an impermeable fault. The analytical and numerical results exhibit a good agreement and thus, confirming the accuracy of the analytical solution. Consequently, this analytical solution could be a useful tool in assessing the reactivation of preexisting faults and thus, the induced seismicity potential during and after injection/pumping into a reservoir.

CODE BRIGHT is the ideal simulator for such kind of verifications because it solves the fully coupled poroelastic problem in a robust and reliable way. In addition, the already verified analytical solution can be used as a benchmark for the verification of other numerical hydromechanical codes.

ACKNOWLEDGMENTS

H.W. would like to acknowledge the financial support received from the Secretariat for Universities and Research of the Ministry of Business and Knowledge of the Government of Catalonia (AGAUR) and the European Social Fund (FI-2019). V.V. acknowledges funding from the European Research Council (ERC) under the European Union's Horizon 2020 Research and Innovation Programme through the Starting Grant GEoREST (www.georest.eu), under grant agreement No. 801809. IDAEA-CSIC is a Center of Excellence Severo Ochoa (Spanish Ministry of Science and Innovation, Project CEX2018-000794-S). M.S. acknowledges financial support from the "HEATSTORE" project (170153-44011), which has been subsidized through the ERANET Cofund GEOTHERMICA (Grant agreement no. 731117), from the European Commission and the Spanish Ministry of Science, Innovation and Universities (PCI2018-092933). F.P. acknowledges funding from the European Union's Horizon 2020 Research and Innovation Programme under Marie Sklodowska-Curie Action ARMISTICE with grant agreement No. 882733.

REFERENCES

[i] Ellsworth, W. L., 2013. Injection-induced earthquakes. Science, 341(6142), 1225942.

[ii] Buijze, L., van den Bogert, P. A., Wassing, B. B., Orlic, B., & ten Veen, J., 2017. Fault reactivation mechanisms and dynamic rupture modelling of depletion-induced seismic events in a Rotliegend gas reservoir. Netherlands Journal of Geosciences, 96(5), s131-s148.

[iii] Van Wees, J., Fokker, P., Van Thienen-Visser, K., Wassing, B., Osinga, S., Orlic, B., . . . Pluymaekers, M., 2017. Geomechanical models for induced seismicity in the Netherlands: inferences from simplified analytical, finite element and rupture model approaches. Netherl. J. Geosc., 96 (5), S183-S202.https://doi.org/10.1017/njg.2017.38.

[iv] Caine, J. S., Evans, J. P., & Forster, C. B., 1996. Fault zone architecture and permeability structure. Geology, 24(11), 1025-1028.

[v] Hansen, O., Gilding, D., Nazarian, B., Osdal, B., Ringrose, P., Kristoffersen, J. B., ... & Hansen, H., 2013. Snøhvit: The history of injecting and storing 1 Mt CO2 in the fluvial Tubåen Fm. Energy Procedia, 37, 3565-3573.

[vi] Ellsworth, W. L., Giardini, D., Townend, J., Ge, S., & Shimamoto, T., 2019. Triggering of the Pohang, Korea, Earthquake (Mw 5.5) by Enhanced Geothermal System Stimulation. Seismological Research Letters, 90(5), 1844-1858.

[vii] Wu, H., Vilarrasa, V., De Simone, S., Saaltink, M. & Parisio, F., 2021. Analytical solution to assess the induced seismicity potential of faults in pressurized and depleted reservoirs. Journal of Geophysical Research: Solid Earth. 126, e2020JB020436.

[viii] Olivella, S., Carrera, J., Gens, A., & Alonso, E. E., 1994. Non-isothermal Multiphase Flow of Brine and Gas through Saline media. Transport in Porous Media, 15, 271:293

[ix] Olivella, S., Gens, A., Carrera, J., & Alonso, E. E., 1996, 'Numerical Formulation for a Simulator (CODE_BRIGHT) for the Coupled Analysis of Saline Media " Engineering Computations, Vol 13, No 7, pp: 87-112.

[x] Eshelby, J. D., 1957. The determination of the elastic field of an ellipsoidal inclusion and related problems. Proc. R. Soc. London, Ser. A, 241, 376-396. http://dx.doi.org/ 10.1098/rspa.1957.0133.

THERMO-HYDRO-MECHANICAL MODELLING OF AQUIFER THERMAL ENERGY STORAGE

Rubén Vidal[*], Sebastià Olivella[*] and Maarten W. Saaltink[*†]

[*] Department of Civil and Environmental Engineering (DECA), School of Civil Engineering, Universitat Politècnica de Catalunya − BarcelonaTech (UPC), UPC Campus Nord, Jordi Girona 1-3, Building D2, 08034 Barcelona, Spain

[†] Associated Unit: Hydrogeology Group (UPC-CSIC), Barcelona, Spain

Key words: HT-ATES, THM Coupled Analysis, Energy, Modelling, Heat transport, Uplift

ABSTRACT. *High Temperature Aquifer Thermal Energy Storage (HT-ATES) can help balance energy demand and supply to make better use of infrastructures and resources. The aim of these systems is to store with wells high amounts of energy in aquifers to reuse it during an energy deficit. HT-ATES require addressing terrain complications such as variations of the properties of the aquifer, thermal losses and the uplift of the surface. Coupled thermo-hydro-mechanical (THM) modelling is a good tool to analyse the viability and cost effectiveness of the HT-ATES systems and to understand the interaction of processes, such as heat flux, groundwater flow and ground deformation. We present the 3D THM modelling of a pilot HT-ATES system, which is inspired by one of the projects of HEATSTORE, a GEOTHERMICA ERA-NET co-funded Project. The results of this study have provided information about heat transport processes, evolution of the energy efficiency and the displacements in the system.*

1 INTRODUCTION

Aquifer Thermal Energy Storage (ATES) consists of several wells that simultaneously inject or extract thermal energy into aquifers. ATES is an efficient and sustainable technology of storing and reusing energy that can contribute to the reduction of greenhouse gas emissions[i]. The aim of ATES is to store the excess energy to reuse it when there is an energy deficit. High-temperature Aquifer Thermal Energy Storage (HT-ATES) provides a good option to store water over 60°C. HT-ATES permits to store heat from industry, waste incineration or power plants and the stored heat can be used directly without heat pumps[ii].

The main obstacles of HT-ATES projects are the precipitation and dissolution of minerals in the wells, variation of the permeability of the aquifer, clogging and corrosion due to microbial activity and unwanted recovery efficiencies[iii]. Problems of stability are important to study. The injection of hot water can cause a local increase in pressure, which coupled to an increase in temperature, it can induce the expansion of the medium[iv]. The increment of pressure and temperature will tend to generate uplift that can reach the surface.

This paper presents the 3D THM modelling of a pilot HT-ATES system. The studied system is inspired by one of the projects of HEATSTORE, which is a GEOTHERMICA ERA-NET co-funded project. The model pretends to simulate the injection of hot water at 90°C in a Central well and the extraction of water in four Auxiliary wells during summer. In

winter, the Auxiliary wells inject water at 50°C and the Central well extract water. The loading lasts longer than the unloading (8 months versus 4 months). More heat is injected than extracted despite the same injection rates are considered during all the year. We make a prediction of the long-term behaviour of the system to see its viability.

The HT-ATES system has been modelled with the Finite Element Method program CODE_BRIGHT, which is a capable of doing coupled thermo-hydro-mechanical analysis in geological media[v].

2 METHODOLOGY

The model represents the fourth part of the real project (Figure 1A). This system is simplified to 2 vertical wells separated 40 m: a Central well and an Auxiliary well. The geological profile consists of a top rock (0 – 400 m depth), an aquifer (400 m – 500 m depth) and a bottom rock (500 m – 600 m depth). Top rock and bottom rock are aquitards (Figure 1B). The modelled wells are octagonal and they are the equivalent of a round well (Figure 1C). The inner part of the wells is empty. The outer part is the well screen and it is very permeable and dispersive with respect the surrounded geological materials in the zone of the injection. The outer part of the wells is the same material as the top rock above the aquifer.

A summary of the main parameters of the geological materials is shown in Table 1. The main difference between the aquitards and the aquifer is the intrinsic permeability. Mechanical properties are the same for all geological materials, except for the well screen at the injection zone. We have considered a linear elastic model for all the materials.

The model boundaries are far enough to capture the behaviour of the problem in the geological media without imposing unrealistic conditions. The size in the horizontal direction is equal to 200 m and the height is 600 m. The length of the wells is 500 m. We have used a semi-structured mesh: unstructured at the top and bottom surfaces and structured in the vertical direction. The elements of the mesh are hexahedral (Figure 1B).

One year of operation has two stages: Injection (0-8 months) and Back Injection (8-12 months). In the Injection, thermal energy is accumulated by injecting a constant flow rate of 25 l/s at 90ºC in the Central well at the same time that we extracted water in the Auxiliary wells. The Back Injection is the energy demand stage. A constant flow rate of 25 l/s at 50ºC is injected in the Auxiliary wells and extracted in the central well simultaneously. The design flow rates are divided by 4 in the model because the geometry corresponds to 1/4 of the domain. We have simulated 10 years of operation or 10 cycles of Injection-Back Injection.

Water is injected and extracted on the external surface of the wells. The total flow rate is converted into a mass flux applied on the well surface. Pressure and temperature are constant on the top surface of the model: atmospheric pressure (0.1 MPa) and 20°C. Restriction of vertical displacements is applied on the bottom surface and a restriction for the lateral displacements is considered at the lateral boundaries of the model. Vertical boundaries and bottom surface are assumed to be impervious. The initial temperature in the entire model is 20^{o}C and the liquid pressure is hydrostatic starting on the upper surface at atmospheric pressure.

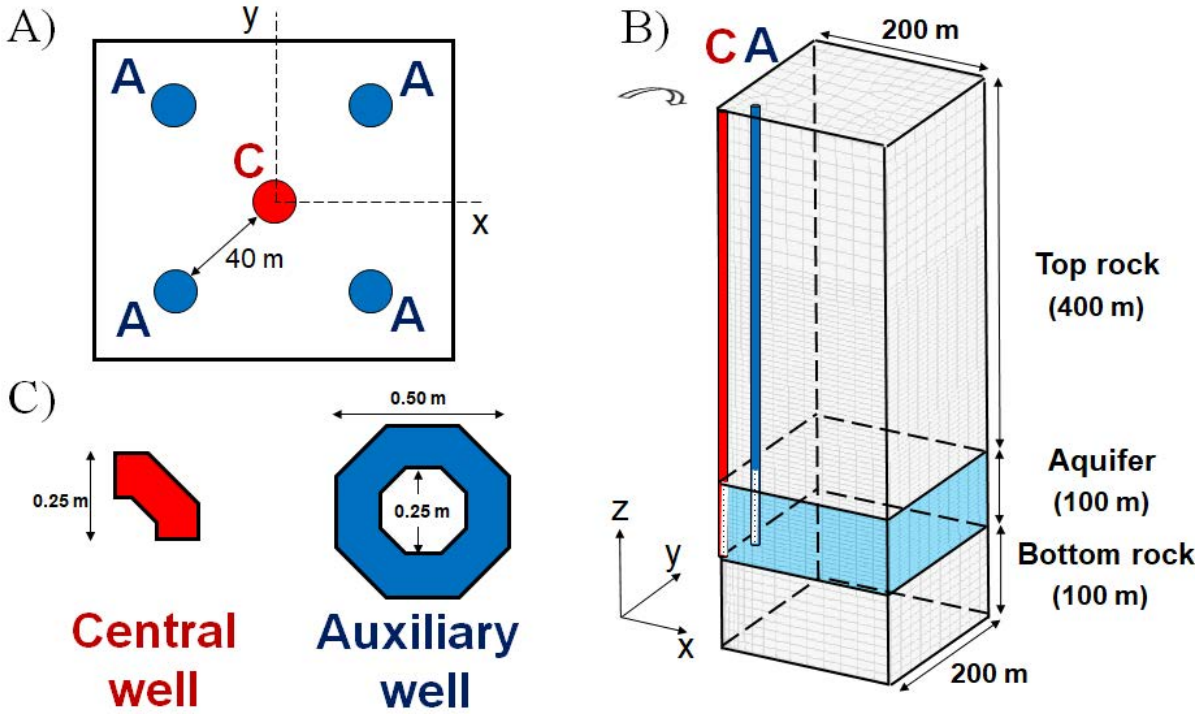

Figure 1. Plant view of all the wells (A), 3D Model (B) and wells geometry for the simulation (C).

Material	Intrinsic permeability (m^2)	Thermal conductivity (W/m·k)	Dispersivities (longitudinal /transversal) (m)	Solid heat capacity (J/ kg·K)	Porosity (-)	Density (kg/m^3)	Elastic Modulus (MPa)	Poisson's ratio (-)
Aquitard	1.0×10^{-16}	2	5/1	1000	0.3	2700	5000	0.3
Aquifer	1.0×10^{-13}	2	5/1	1000	0.3	2700	5000	0.3
Well screen	1.0×10^{-9}	2	100/10	1000	0.3	2700	500	0.3

Table 1. Material properties.

3 RESULTS

The injection of thermal energy in the aquifer causes an increment of the liquid pressure and temperature. The liquid pressure is higher in the well that we inject hot water in each stage. Thus, water flows from the injection well to the extraction well (Figure 2A). During one year of simulation, the thermal energy concentrates around the central well. The temperature is always higher in the central well than in the auxiliary wells in the aquifer (Figure 2B).

Thermal radius is a first calculation to obtain the volume of the aquifer affected only by the advection generated by the injection of hot water[vi]. In this system, the thermal radius is 47 m at the end of the Injection. This distance is quite similar as the separation between the Central well and the Auxiliary well, which is 40 m. In the model, if we suppose that the affected

aquifer is cylindrical, the thermal radius is 68 m (Figure 3). The difference between the hand calculated thermal radius and the modelled thermal radius is that the dispersion and conduction play an important role in the second case. The modelled thermal radius increases with time and it reaches 140 m for 10 years (Figure 3).

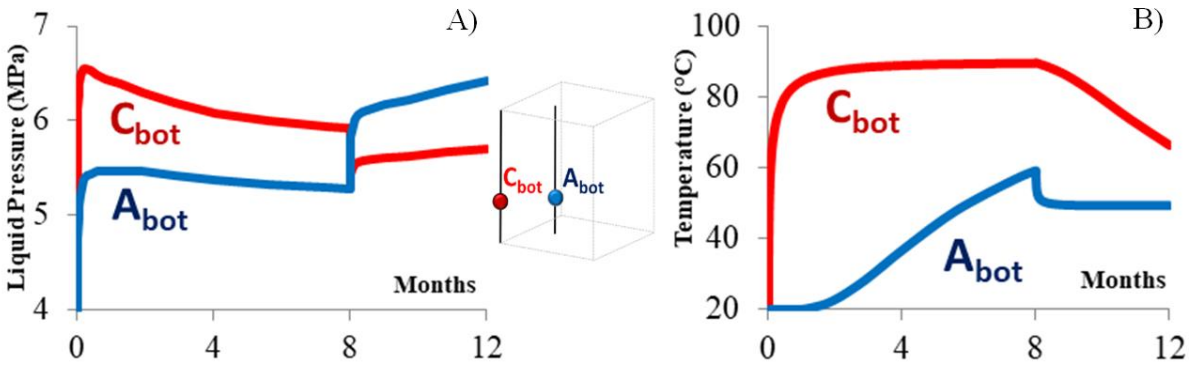

Figure 2. Liquid pressure (A) and Temperatures (B) in the wells in the aquifer.

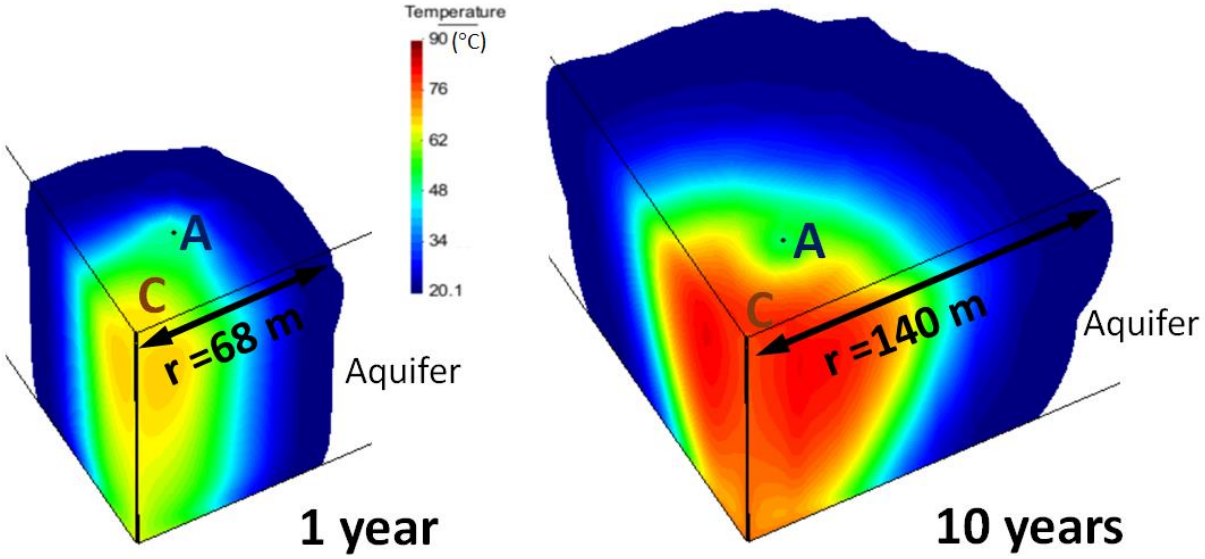

Figure 3. Isotherms in the aquifer for 1 year and 10 years

The energy recovery factor is the ratio between the extracted energy and the injected energy[vii]. This factor can help know the efficiency of the geothermal system. In the studied system, the energy recovery factor in the Back Injection is twice that in the Injection for the first year (Figure 4). The energy recovery factor increases to 0.89 asymptotically for 10 years of operation.

The dimensionless Rayleigh number Ra is the ratio between the conductive transport characteristic time and the buoyant thermal transport characteristic time. The Ra for the model is 20.7 for the Injection. The Ra of the model is lower than the critical Ra_c, which is $4\pi^2$ according to Lapwood[viii]. Thus, thermal conduction dominates over the free convection in the

aquifer. If free convection were dominant, the stored energy will tend to concentrate on the top of the aquifer and the energy efficiency of the system would be lower.

The strains are result of both hydraulic and thermal loads. These loads are consequence of the injection of hot water. The maximum vertical displacements of the model are located on the surface (Figure 5). The uplift is concentrated between the Central well and the Auxiliary well and it is reduced with distance from the center of the system. The maximum displacements are reached at the end of the year. The vertical displacements for 10 years are approximately the same as for 1 year, because we have considered linear elastic model for all the materials. Very low horizontal displacements (lower than 1 mm) have been obtained on the surface because of the symmetry of the studied problem.

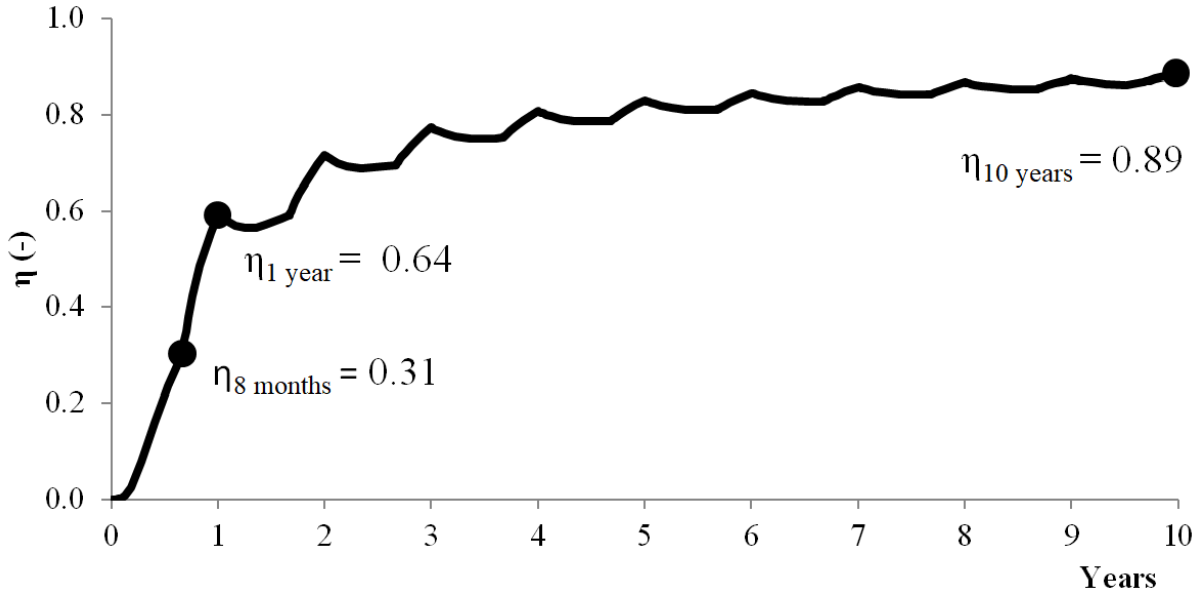

Figure 4. Energy recovery factor for 10 years of operation.

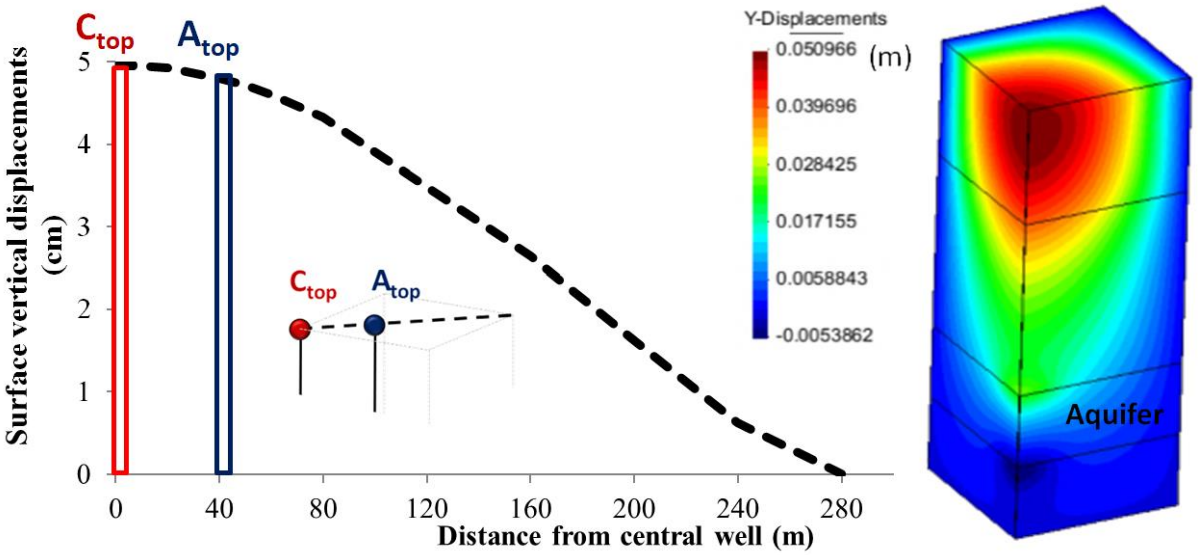

Figure 5. Vertical displacements.

4 CONCLUSIONS

HT-ATES is a hopeful technology that requires the study of the underground THM processes. The studied HT-ATES system consists of one Central well and four Auxiliary wells. In one year of operation, it is accumulated energy during 8 months and, then, it is extracted during the last 4 months. Advection, dispersion and conduction are significant heat transport processes in the aquifer. Thermal conduction dominates over the free convection which produces favourable energy efficiencies. The energy recovery factor of the system increases more in the Back Injection, when there is a demand of energy, than during the Injection. The system is more efficient in terms of energy recovery, the more years the system is operating. Both thermal loads and hydraulic loads have an important role in the displacements that take place in the aquifer. Uplift is concentrated near the Central well on the surface.

REFERENCES

[i] Bloemendal, M., Olsthoorn, T., Boons, F., 2014. How to achieve optimal and sustainable use of the subsurface for Aquifer Thermal Energy Storage. *Energy Policy* 66, 104–114.

[ii] Drijver, B., Mastijn van Aarssen, M., Bas de Zwart, 2012. High-temperature aquifer thermal energy storage (HT-ATES): sustainable and muti-usable. Innostock 2012. *The 12th International Conference on Energy Storage*.

[iii] Snijders, A.L., 2000. Lessons from 100 ATES projects – The developments of aquifer storage in the Netherlands. *Proccedings TERRASTOCK 2000, Stuttgart, Germany*.

[iv] Rutqvist J., Barr, D., Datta, R., Gens, A., Millard, A., S. Olivella, S., Tsang, C.-F., Tsang, Y., 2005. Coupled thermal–hydrological–mechanical analyses of the Yucca Mountain Drift Scale Test—Comparison of field measurements to predictions of four different numerical models. 2005. *International Journal of Rock Mechanics and Mining Sciences*, 42, 680-697.

[v] Olivella, S., A. Gens, J. Carrera, E. E. Alonso, 1996, Numerical Formulation for a Simulator (CODE_BRIGHT) for the Coupled Analysis of Saline Media. *Engineering Computations*, Vol 13, No 7, pp: 87-112.

[vi] Sommer, W., Valstar, J., Leusbrock, I., Grotenhuis,T., Rijnaarts, H., 2015. Optimization and spatial pattern of large-scale aquifer thermal energy storage. *Applied Energy.*

[vii] Doughty, C., Hellström, G., Tsang, C.F., 1982. A Dimensionless Parameter Approach to the Thermal Behavior of an Aquifer Thermal Energy Storage System. *Water Resources Research*, Vol. 18, No 3, Pages 571-587, June 1982.

[viii] Schout, G., Drijver, B., Gutierrez-Neri, M., Schotting, R., 2014. Analysis of recovery efficiency in high-temperature aquifer thermal energy storage: a Rayleigh-based method. *Hydrogeology Journal* 22 (1), 281–291.

MODELLING THE EFFECT OF IN-SOIL TEMPERATURE AND RELATIVE HUMIDITY ON PERFORMANCE OF PET STRAP SOIL REINFORCEMENT PRODUCTS

A. Moncada[*], I.P. Damians[*†], S. Olivella[*†] and R.J. Bathurst[§]

* Department of Civil and Environmental Engineering (DECA), Universitat Politècnica de Catalunya·BarcelonaTech (UPC); Campus Nord UPC, 08034 Barcelona, Spain
Email : anibal.moncada@estudiantat.upc.edu

† International Centre for Numerical Methods in Engineering (CIMNE)
Campus Nord UPC, 08034 Barcelona, Spain (http://www.cimne.com)

§ Geoengineering Centre at Queen's-RMC, Civil Engineering Department, Royal Military College of Canada, Canada

Key words: Reinforced soil walls, Polyester straps, THM modelling, in-soil temperature and relative humidity distributions

Abstract. *Polyester (PET) strap reinforcement materials are now used routinely as soil reinforcement for mechanically stabilized earth (MSE) walls. Strength and stiffness of the polyester fibres can be expected to decrease with increasing temperature and in the presence of moisture. This study presents the results of analyses using numerical simulations that were carried out to estimate, first, the in-soil temperature and relative humidity changes for different ground properties and atmospheric boundary conditions, and second, the temporal strength and stiffness changes in simulated buried PET straps placed in different soil environments while subjected to different tensile loads and temperatures.*

1 INTRODUCTION

In mechanically stabilized earth structures, the crucial role of temperature and relative humidity on the mechanical and chemical degradation of polyester (PET) fibres due to hydrolysis is well documented in the literature [i], [ii]. Strength and stiffness of the polyester fibres can be expected to decrease with increasing temperature and in the presence of moisture. These reductions modify the partial factor for creep and chemical degradation that is used in internal stability limit state design for PET strap MSE walls. Hence, local ambient conditions should be accounted for at the design phase.

In order to analyze the long-term behaviour of PET straps, the present study proposes a coupled finite element model based on the software CODE_BRIGHT [iii] in which the in-soil distribution of temperature and relative humidity for different atmospheric conditions are evaluated first. Next, visco-elastic and visco-plastic models are implemented to simulate PET strap long-term response calibrated using the laboratory results of You-Kyum et al. [iv] for GECO's FASTEN FS products [v]. Finally, a linear coupled thermo-hydro-mechanical (THM) MSE wall 2D model is proposed as a preliminary approach.

2 NUMERICAL MODEL

The geometry of the thermal-hydro coupled (TH) model is presented in Figure 1 (5536 structural quadrilateral elements with 5714 nodes). Mesh construction included all mechanical elements such as the 1.5 m-high concrete facing panels, the 20 mm-thick bearing pads and the

3 mm-thick PET reinforcement layers with 0.7H length. The water table was located at 10 m depth below the ground surface at the wall. The bottom base temperature was constant at +2°C higher than the mean annual temperature reported from the temperature registry used for each analysis. Staged construction was not used in this study to simplify the model.

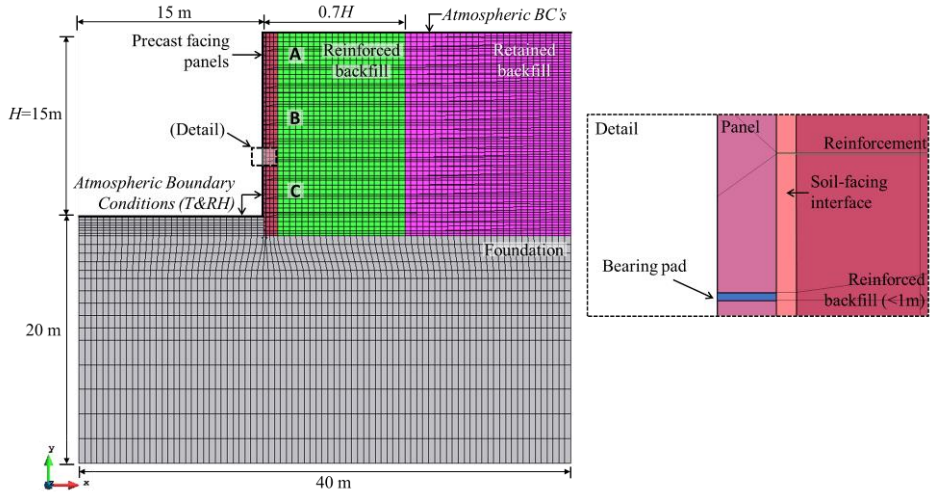

Figure 1: 2D model domain and finite element mesh used for analyses.

Boundary conditions (BC) consist of ambient in-air data records including actual real time series input data of temperature (T) and relative humidity (RH) for each control location [vi] over the upper boundary. Points A, B and C, located 2 m from facing and at 1, 7 and 14 m-depth, respectively, were used as measuring points to compare results. Four different geographic locations corresponding to continental (Toronto), Mediterranean (Barcelona), desert (Abu Dhabi) and tropical (Singapore) climates were considered. Analyses for each model were for 1-, 3- and 5-year periods using daily records from years 2016 through 2020.

A granular soil was considered in this study. Soil thermal dispersion is modeled by Fick´s law with horizontal and vertical dispersivity of d_l = 5 m and d_t = 0.5 m. Thermal conductivity was modelled using Fourier´s law, with dry and saturated conductivity values of γ_{dry} = 0.5 W/mK and γ_{sat} = 1 W/mK. Default values for solid phase specific heat (c_s = 1000 $Jkg^{-1}K^{-1}$) and density (ρ_s = 2700 kgm^{-3}) were used. Water retention curve (Van Genuchten model) for soil and concrete facing panels was modelled with a reference pressure P_0 = 0.005 MPa and P_0 = 0.001 MPa and shape parameter λ = 0.8 and λ = 0.4 respectively. Values for the PET strap reinforcement layers, precast facing panels and HDPE bearing pads have been adjusted to equivalent values for a 2D plane strain 1-m slice. Initial porosity values of ϕ_0 = 0.3, ϕ_0 = 0.15, ϕ_0 = 0.01 and ϕ_0 = 0.4 and intrinsic permeability values of $K = 1\times10^{-12}$, $K = 1\times10^{-12}$, $K = 1\times10^{-16}$ and $K = 1\times10^{-10}$ were considered for soil, precast facing panels, PET strap reinforcement layers and HDPE materials

In order to simulate in-soil conditions acting over the PET strap reinforcement, temperature- and saturation-dependent visco-elastic (VE) and vico-plastic (VP) constitutive models were used to account for creep and strain softening over long-term constant load, respectively. The mechanical parameters used to model the PET straps are presented in Table 1. Stiffness was calculating considering an average width of 89 mm per strap and two connections every 2.5 m in the wall face direction. A linear model with an elastic modulus E=32 GPa and Poisson´s ratio ν=0.2 was used for the precast concrete facing panels. Two

scenarios were analyzed. First, elements with bi-linear elastic moduli and VE properties were subjected to an initial tension, followed by a ramp increase up to the desired load representing a selected fraction of the ultimate tensile strength (UTS). Second, elements with linear elastic modulus, VE and VP properties were subjected to a constant initial load.

Table 1: Model parameters for PET strap reinforcement.

Constitutive model	Parameter	Value
Linear elasticity	Elastic modulus, E [MPa]	2.2 − 4.8
	Poisson's ratio, ν [-]	0.30 − 0.34
Bi-linear elasticity	1st elastic modulus, E_1 [MPa]	1.7 − 3.9
	2nd elastic modulus, E_2 [MPa]	45 – 100
	Poisson ratio, ν [-]	0.20 − 0.33
	Volumetric strain limit for E_i change, $\varepsilon_{v\text{-limit}}$ [-]	0.0078 − 0.086
Visco-elasticity (VE)	Fluidity, B [$s^{-1}MPa^{-1}$]	$5.3\times10^{-14} - 2.1\times10^{-10}$
Visco-plasticity (VP)	Power of stress function, m [-]	2.6 − 3.8
	Fluidity, Γ [$s^{-1}MPa^{-m}$]	$3.6\times10^{-4} - 1.4\times10^{-3}$
	Softening parameter, η^*, [-]	$1\times10^{-3} - 8\times10^{-2}$
	Peak & residual adhesion parameters, a_{peak} & $a_{res.}$ [MPa]	0.05−0.12 & 0.03−0.12
	Peak & residual friction parameters, δ_{peak} & $\delta_{residual}$ [°]	1×10^{-4} & 1×10^{-5}

3 RESULTS

3.1 Atmospheric effect modelling

Figure 2 and Figure 3 show T and RH distribution over a 1-year analysis period for Barcelona 2020 in-air (atmospheric) conditions. Model results show an important variation of temperature within the first 2 meters from the domain air boundaries, followed by a 4-meter zone in which variations are visible but less pronounced. As depth increases, in-soil T appears to remain unaffected and converges to the imposed lower BC. Regarding RH, a zone of influence of 1 m can be identified at the air boundaries. At depth, RH reaches saturation near the imposed water table. Depending on the observation period, the backfill as a whole, shifts from a saturated air condition to RH values as low as 50%, Due to the open joints between panels (2 bearing pads per panel) propagation zones due to diffusive flow through these openings can be seen.

Figure 4 shows the variation of T and RH at points A, B and C for all locations ambient air conditions. As depth increases, variations in T go from 10°C at 1 meter to a stable 4°C variation at 14 and 21 meters for all but Singapore, which remains at a steady 29°C at all observation points. As depth increases the peaks of T and RH distribution curves are present at a later time with respect to surface values. Mean in-soil T and RH values were 29°C, 17°C, 28°C, and 10°C and 59%, 86%, 85% and 84% for Abu Dhabi, Barcelona, Singapore, and Toronto, respectively over a 1-year analysis. Results show air saturation (RH = 100%) occurs for periods of 100 days or more during the one-year cycle for Barcelona and Toronto. RH tends to higher values as depth increases. Increases of RH within the soil due to lower temperatures can be observed. It must be noted that the current model does not account for surface precipitation which could potentially change the in-soil T and RH distributions.

Figure 5 shows the temperature variation of a vertical soil profile at 4 meters from the wall facing over a 5-year period using the Barcelona registry. Results show that T changes within the first 3 meters constitute the largest fluctuations matching the prescribed BC (3°C to 30°C). From 3 to 15 meter-depth, T fluctuations diminish to ±2°C oscillations with respect to the annual mean atmospheric temperature (17°C). Below 15 meters, T stabilizes with less than ±1°C variation and approaches a constant value matching the lower BC.

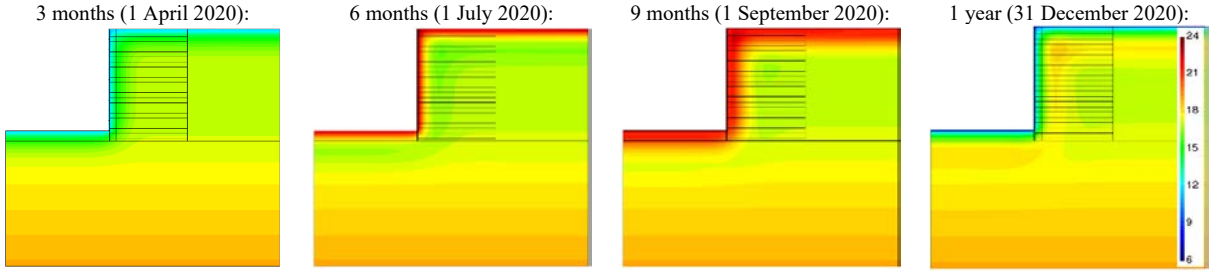

Figure 2: TH model 1-year temperature (ºC) results for Barcelona 2020.

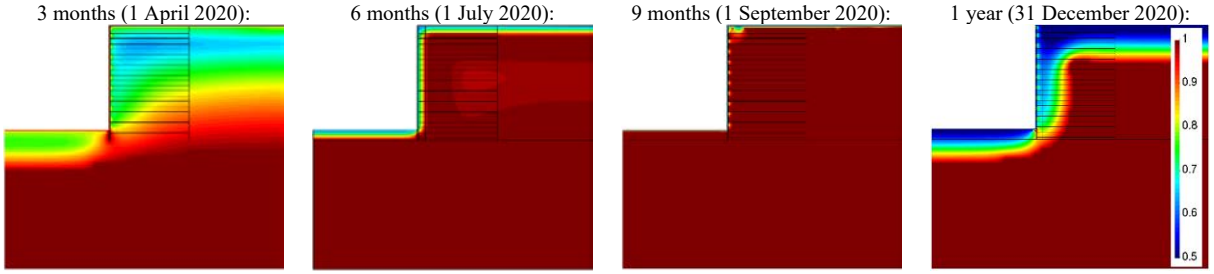

Figure 3: TH model 1-year relative humidity (-) results for Barcelona 2020

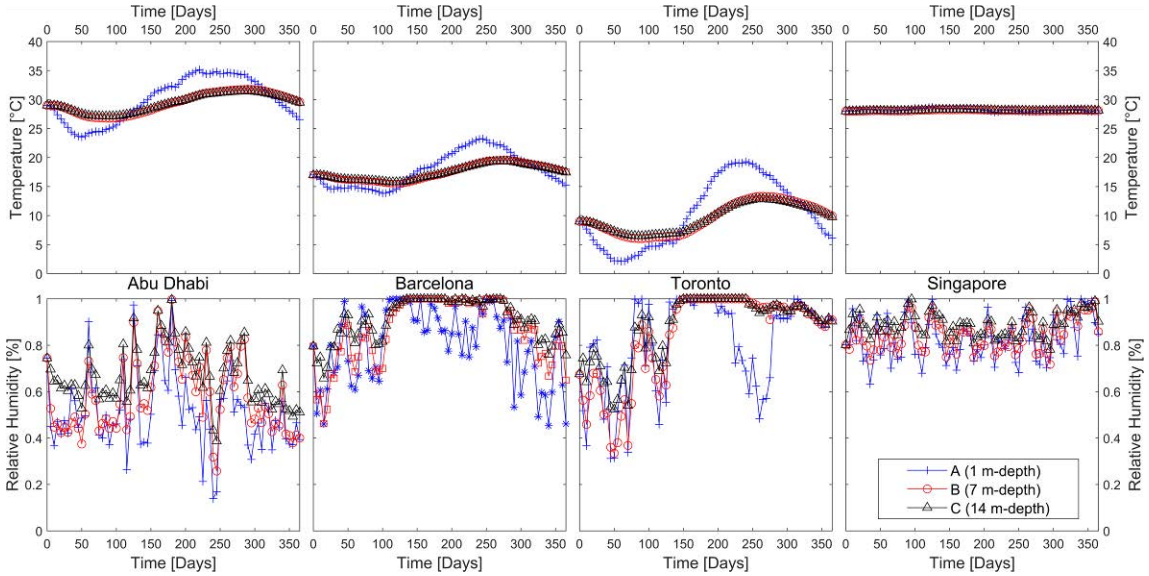

Figure 4: Evolution of temperature and relative humidity at points A, Band C for the four different locations and climates considered

3.2 PET strap modelling

Figure 6 depicts the adjustment of the proposed models with creep laboratory measurements for grade 30, 50 and 70 kN straps under loads of 66% and 70% of UTS. The obtained adjustment is adequate for both the bi-linear elastic and VE models, and VE and VP models. Figure 7 illustrates the influence of temperature on creep behaviour for a grade 30 reinforcement material under 70% UTS load at constant T. Temperatures correspond to the maximum and minimum mean values obtained using the TH models with different ambient in-air conditions. Due to temperature variations, the VE and VP models update their equivalent fluidity, thus, long-term deformation varies within a range of 1-1.5% for a 19°C variation over a 50-year period. By including a linear expansive model, an initial change in

temperature (from 20°C to 10°C or 20°C to 29°C), followed by a constant temperature modelling, shifts the creep curve to higher or lower deformation for increasing or decreasing temperatures, respectively.

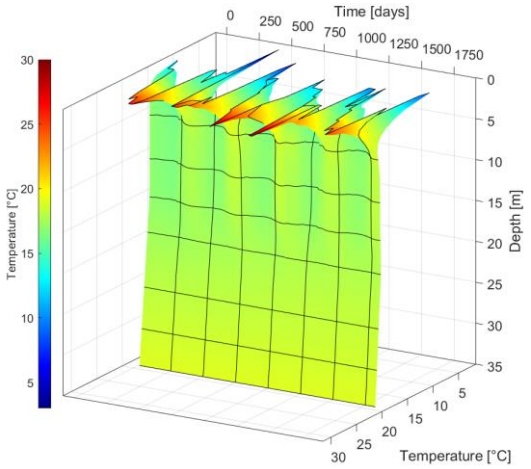

Figure 5: In-soil temperature distribution over a 5-year period using Barcelona climate data and sand backfill model

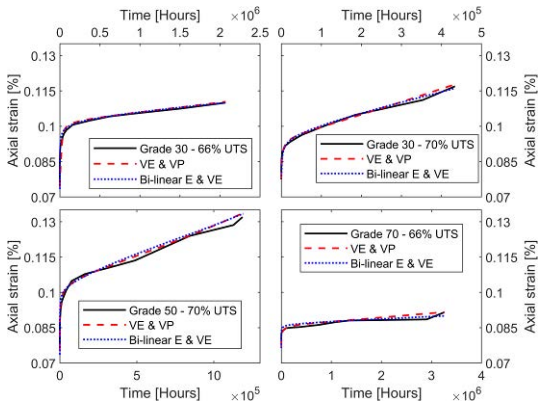

Figure 6: Long-term deformation model results for grades 30, 50 and 70 kN at 66 or 70% of UTS load compared to accelerated laboratory creep tests.

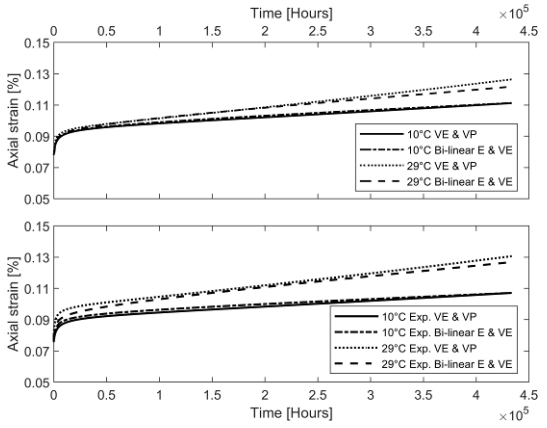

Figure 7: Creep behavior changes due to temperature variations from 20°C to 10°C or 29°C for a grade 30 strap at 70% UTS load.

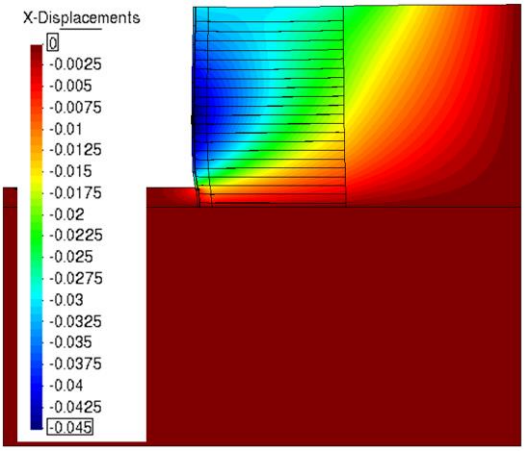

Figure 8: Horizontal outward displacements (m) and deformed mesh (amplification factor ×10) after 1 year analysis with an elastic coupled THM model with PET straps reinforcements (bi-linear elastic and VE model) using Barcelona 2020 atmospheric registry.

Figure 8 presents horizontal displacements of the deformed mesh for a 1-year analysis period using Barcelona atmospheric BC with the bi-linear elastic and VE PET strap model together with linear elastic concrete and backfill materials. Since the analysis is limited to one year, no significant variations were observed between different BC cases. When comparing linear elastic and VE model results, the maximum displacement increases by about 4% over a 1-year period for the VE model.

4 CONCLUSIONS

- A 2D THM model was implemented to evaluate the effects of prolonged ambient conditions on in-soil T and RH distributions on the backfill soil and long-term behaviour of the embedded PET strap reinforcement layers used in MSE walls with different ambient environmental conditions.
- TH models gave results in accordance with previous studies [vii], [viii] for temperature distributions in-soil as a function of depth. The mean in-soil T can be approximated by the annual mean environmental (atmospheric) in-air values.
- Air saturation was achieved for over 100 days for Barcelona and Toronto climate registry cases, with mean values of 86% and 84%, respectively. For desert conditions (Abu Dhabi), air saturation was rarely observed (mean RH = 59%). Tropical conditions (Singapore) resulted in an almost constant RH = 85%.
- VE and VP models were fitted to creep master curves with satisfactory results for different grades of PET straps and UTS loads, incorporating T dependencies.

ACKNOWLEDGEMENTS

The authors wish to thank Aaron Kim from GECO Industrial (Korea, Rep) for providing data for polymeric straps (FASTEN products) from reliability assessment testing records.

REFERENCES

[i] Jailloux, J.M., Nait-Ali, K.L., and Freitag, N. 2008. Exhaustive long-term study on hydrolysis of high-tenacity polyester–10-year results. In Proceedings of the 4th European Geosynthetics Conference, Edinburgh, UK, 6p.(CD-ROM–Paper 212).

[ii] Greenwood, J.H., Schroeder, H.F., and Voskamp, W.; 2012. Durability of Geosynthetics (Publication 243). CUR Committee C 187. Building and Infrastructure. ISBN 978-90-376-0533-4.

[iii] Olivella S, Gens A, Carrera J, Alonso E. 1996 Numerical formulation for a simulator (CODE_BRIGHT) for the coupled analysis of saline media. Engineering Computations 13(7), 87-112.

[iv] You-Kyum, K., Gyeong-Yun, S. 2018. Reliability assessment of polymeric straps (FASTEN FS) for soil reinforcement. H411-18-00067. GECO Industrial Co., Ltd. FITI Testing and Research Institute, Chungbuk, Korea.

[v] GECO 2021. GECO Industrial Co., Ltd. Gyeonggi-do, Republic of Korea. http://gecoind.com/en/product/fasten.php

[vi] WeatherOnline Ltd. Meteorological Services, viewed on March 2021, https://www.weatheronline.co.uk/

[vii] Kasozi, A.M., Siddharthan, R.V., and Mahamud, R. 2015. Temperature distribution in mechanically stabilized earth wall soil backfills for design under elevated temperature conditions. Journal of Thermal Science and Engineering Applications, 7(2).

[viii] Segrestin, P., and Jailloux, J.M. 1988. Temperature in soils and its effect on the ageing of synthetic materials. Geotex and Geomem, 7, 51-69.